# Coupled double-distribution-function lattice Boltzmann method for the compressible Navier-Stokes equations

Q. Li, Y. L. He,* Y. Wang, and W. Q. Tao
*State Key Laboratory of Multiphase Flow, School of Energy and Power Engineering, Xi'an Jiaotong University, Xi'an, Shaanxi 710049, China*

(Received 15 July 2007; revised manuscript received 10 September 2007; published 16 November 2007)

A coupled double-distribution-function lattice Boltzmann method is developed for the compressible Navier-Stokes equations. Different from existing thermal lattice Boltzmann methods, this method can recover the compressible Navier-Stokes equations with a flexible specific-heat ratio and Prandtl number. In the method, a density distribution function based on a multispeed lattice is used to recover the compressible continuity and momentum equations, while the compressible energy equation is recovered by an energy distribution function. The energy distribution function is then coupled to the density distribution function via the thermal equation of state. In order to obtain an adjustable specific-heat ratio, a constant related to the specific-heat ratio is introduced into the equilibrium energy distribution function. Two different coupled double-distribution-function lattice Boltzmann models are also proposed in the paper. Numerical simulations are performed for the Riemann problem, the double-Mach-reflection problem, and the Couette flow with a range of specific-heat ratios and Prandtl numbers. The numerical results are found to be in excellent agreement with analytical and/or other solutions.

DOI: 10.1103/PhysRevE.76.056705 PACS number(s): 47.11.−j, 05.50.+q, 47.40.−x

## I. INTRODUCTION

In the past two decades or so, the lattice Boltzmann method (LBM) has been developed into an alternative numerical method to simulate fluid flows and model physics in fluids [1–3]. Unlike the conventional numerical methods, which are based on discretization of macroscopic governing equations, and unlike the molecular dynamics method, which is based on molecular representation with complicated molecule collision rules, the LBM is based on microscopic models and mesoscopic kinetic equations for particle distribution functions; it simulates fluid flows by tracking the evolutions of the distribution functions and then accumulates the distributions to obtain macroscopic averaged properties. An attractive feature of the LBM is its handling of complicated geometries such as porous media flow where wall boundaries are extremely irregular. Other merits of the LBM are the localization and easy implementation of its computational scheme, and the LBM computations tend to be easily parallelized.

Although the LBM has achieved great success in simulating nearly incompressible and isothermal fluid flows, it has not been able to handle realistic thermal compressible flows with enough satisfaction. As reported in Ref. [4], the current thermal lattice Boltzmann models can be generally classified into three categories. The first category is the passive-scalar approach [5,6]. It utilizes the fact that the macroscopic temperature satisfies the same evolution equation as a passive scalar if the viscous heat dissipation and the compression work done by the pressure can be neglected. In this case, the temperature is advected by the flow velocity but does not affect the flow field. Then the temperature field is simulated by a new scalar density distribution function.

The second category includes several energy-conserving approaches, such as the multispeed approach [7–12], the hybrid approach [4,13], and the double-distribution-function (DDF) approach [14–18]. The multispeed approach is a straightforward extension of the common isothermal lattice Boltzmann models in which only the density distribution function is used. To obtain the energy equation at the macroscopic level, additional particle speeds are necessary and the equilibrium distribution functions must include higher-order velocity terms. The multispeed models usually suffer severe numerical instability and a narrow range of temperature variation. Moreover, the Prandtl number is usually fixed at constant and the specific-heat ratio cannot be chosen freely. Although these two problems have been solved respectively by some later models [10,11], these models are more complicated (compared with previous multispeed models) and the model which can simultaneously solves the two problems has seemingly not been found yet. In the hybrid approach, the flow simulation is decoupled from the solution of the temperature equation. Specially, the flow simulation is accomplished by the LBM, while the temperature field is solved by conventional numerical methods, such as the finite-difference method.

The first DDF model was devised by He *et al.* [14]; this model is based on the principle that the isothermal lattice Boltzmann models can be directly derived by properly discretizing the continuous Boltzmann equation in temporal, spatial, and the particle velocity spaces. Following the same procedure, an internal energy distribution function model can be derived by discretizing the continuous evolution equation for the internal energy distribution, and then two different distributions are obtained, one for the flow field and the other for the temperature flied. This model has attracted much attention since its emergence for its excellent numerical stability and adjustability of the Prandtl number. However, this model includes complicated gradient terms involving tempo-

*Corresponding author. yalinghe@mail.xjtu.edu.cn

 

ral and spatial derivatives of the macroscopic flow variables, which may introduce some additional errors and do harm to the numerical stability. Several improved models have been proposed to overcome these drawbacks [16,17]. Unfortunately, complicated gradient terms will still exist if the viscous heat dissipation and the compression work are taken into account. Recently, Guo *et al.* [18] proposed another version by introducing a total energy distribution function to replace the internal energy distribution function. Such a choice not only enables the thermal lattice Boltzmann models to be simple but also makes the inclusion of compression work and viscous heat dissipation to be easier. Nevertheless, the model devised in Ref. [18] is a decoupling model in which the energy equation is decoupled from the momentum equation. In other words, the temperature field does not affect the flow field. Then the pressure and velocity fields can be established without referring to the energy equation.

The last category includes various shock-capturing schemes based on the LBM to treat fully compressible Euler [19–22] or Navier-Stokes (NS) equations [23–28]. Among these models, a locally adaptive lattice Boltzmann model was devised by Sun and Hsu [24–28]. In this model, the lattice velocities are chosen according to the local flow velocity and internal energy, and then the fluid velocity is no longer limited by the lattice velocities. So it permits the mean flow to have high Mach number. Although the streaming-collision procedure is still used in this model, the particles are no longer simply hopping from one grid point to the next, because the advection step is adopted to the local flow velocity in order to allow large speeds. Therefore, a reconstruction step is necessary to obtain the values on the grid nodes and interpolations have to be used, which will introduce undesirable numerical artifacts [4]. Moreover, the relaxation time $\tau$ is fixed at 1 and the Prandtl number is equal to the specific-heat ratio, which may limit its application. Recently, Qu *et al.* [22] proposed an alternative lattice Boltzmann method to construct equilibrium distribution functions for inviscid compressible flows at high Mach number, and the conventional Maxwellian distribution function is replaced by a circular function in this method. However, one of the constraints to recover the macroscopic equations is not completely satisfied, which may cause some problems when the method is directly extended for the viscous compressible flows, and the Prandtl number is also equal to the specific-heat ratio in this method.

Despite many brilliant attempts, to date, there is still lack of a lattice Boltzmann model which can make both the specific-heat ratio and the Prandtl number arbitrary for the compressible NS equations. Among the approaches and models mentioned above, we especially appreciate the numerical stability and the adjustability of the Prandtl number in the DDF approach. And we also note that the multispeed approach can recover the compressible momentum and energy equations with appropriate discrete velocities. In addition, much research has showed that discontinuity-capturing schemes should be used to solve the differential form of the lattice Boltzmann equation in order to capture discontinuities in the compressible flows. On the basis of the above considerations, we aim to propose a lattice Boltzmann method for the compressible NS equations with a flexible specific-heat ratio and Prandtl number by combining the DDF approach with the multispeed approach. In the method, a density distribution function based on a multispeed lattice is used to recover the compressible continuity and momentum equations, while the energy equation is recovered by an energy distribution function and its evolution equation. The two distribution functions can be coupled together by using the thermal equation of state. For the purpose of obtaining an adjustable specific-heat ratio, a constant related to the specific-heat ratio will appear in the equilibrium energy distribution function. Furthermore, in order to improve the numerical accuracy and stability, an implicit-explicit (IMEX) finite-difference numerical technique [29–31], is introduced to solve the Boltzmann equations in the coupled DDF method.

The rest of this paper is organized as follows. In Sec. II, a coupled DDF lattice Boltzmann method with a flexible specific-heat ratio and Prandtl number is described. In particular, two different coupled DDF models are constructed there. In Sec. III, the implicit-explicit finite-difference numerical technique is introduced. In Sec. IV, numerical tests of the coupled DDF models are performed for the Riemann problem, the double-Mach-reflection problem, and the Couette flow. Finally, a brief conclusion is given in Sec. V.

## II. COUPLED DOUBLE-DISTRIBUTION-FUNCTION LATTICE BOLTZMANN METHOD

### A. Density distribution function for the compressible continuity and momentum equations

In this subsection, a density distribution function to recover the compressible continuity and momentum equations will be derived. It is different from the density distribution functions which are employed to recover all the macroscopic equations in the multispeed approach and also different from those used in the previous DDF models which cannot recover the compressible momentum equation correctly. We start with the following discrete Boltzmann Bhatnagar-Gross-Krook (BGK) [33,34] equation:

$$\frac{\partial f_\alpha}{\partial t} + (\boldsymbol{e}_\alpha \cdot \nabla) f_\alpha = -\frac{1}{\tau_f}(f_\alpha - f_\alpha^{eq}) \quad (\alpha = 1,2,\ldots,\mathcal{N}), \tag{1}$$

where $f_\alpha(t,\boldsymbol{r},\boldsymbol{e}_\alpha)$ is the density distribution function [in the equation we drop the dependence on $(t,\boldsymbol{r},\boldsymbol{e}_\alpha)$ for simplicity] and $f_\alpha^{eq}$ is its corresponding equilibrium distribution function. The symbol $t$ is the time, $\boldsymbol{r}$ is the particle position, $\boldsymbol{e}_\alpha$ is the discrete particle velocity along the $\alpha$th direction, $\mathcal{N}$ is the total number of discrete velocity directions, $\nabla = \partial/\partial \boldsymbol{r}$ is the Hamiltonian operator, and $\tau_f$ is the relaxation time for the momentum transport. The macroscopic quantities—density $\rho$ and velocity $\boldsymbol{u}$—are defined as

$$\rho = \sum_\alpha f_\alpha, \tag{2a}$$

$$\rho \boldsymbol{u} = \sum_\alpha f_\alpha \boldsymbol{e}_\alpha. \tag{2b}$$

The equilibrium density distribution function should satisfy the following velocity moment condition to recover the compressible continuity and momentum equations:

$$\sum_{\alpha} f_{\alpha}^{eq} = \rho, \tag{3a}$$

$$\sum_{\alpha} f_{\alpha}^{eq} e_{\alpha i} = \rho u_i, \tag{3b}$$

$$\sum_{\alpha} f_{\alpha}^{eq} e_{\alpha i} e_{\alpha j} = \rho u_i u_j + p\delta_{ij}, \tag{3c}$$

$$\sum_{\alpha} f_{\alpha}^{eq} e_{\alpha i} e_{\alpha j} e_{\alpha k} = \rho u_i u_j u_k + p(u_k \delta_{ij} + u_j \delta_{ik} + u_i \delta_{jk}), \tag{3d}$$

$$\sum_{\alpha} f_{\alpha}^{eq} e_{\alpha}^2 = \rho u^2 + Dp, \tag{3e}$$

$$\sum_{\alpha} f_{\alpha}^{eq} e_{\alpha}^2 e_{\alpha i} = [\rho u^2 + (D+2)p]u_i, \tag{3f}$$

where $p$ is the pressure and $D$ is the dimension of the space and the subscripts $i$, $j$, and $k$ indicate the $x$, $y$, or $z$ component. $e_{\alpha}^2 = \boldsymbol{e}_{\alpha} \cdot \boldsymbol{e}_{\alpha}$, and $\delta_{ij}$, $\delta_{ik}$, and $\delta_{jk}$ are the Kronecker delta functions.

The compressible continuity and momentum equations can be derived through the Chapman-Enskog expansion. By introducing the multiscale expansions, we expand the space derivative, the time derivative, and the density distribution function, respectively, as

$$\boldsymbol{\nabla} = K\boldsymbol{\nabla}_1, \tag{4a}$$

$$\frac{\partial}{\partial t} = K\frac{\partial}{\partial t_1} + K^2\frac{\partial}{\partial t_2} + \cdots, \tag{4b}$$

$$f_{\alpha} = f_{\alpha}^{eq} + Kf_{\alpha}^{(1)} + K^2 f_{\alpha}^{(2)} + \cdots, \tag{4c}$$

where $K$ is a small parameter proportional to the Knudsen number. Combining Eqs. (2a), (2b), (3a), and (3b), we can obtain

$$\sum_{\alpha} f_{\alpha}^{(n)} = 0, \quad \sum_{\alpha} f_{\alpha}^{(n)} \boldsymbol{e}_{\alpha} = 0, \quad n = 1,2, \ldots . \tag{5}$$

If we assume that the pressure is defined as

$$p = \frac{1}{D}\left(\sum_{\alpha} f_{\alpha} e_{\alpha}^2 - \rho u^2\right), \tag{6}$$

then the following equation can be obtained by combining Eq. (3e) with Eq. (6):

$$\sum_{\alpha} f_{\alpha}^{(n)} e_{\alpha}^2 = 0. \tag{7}$$

Substituting Eqs. (4a)–(4c) into Eq. (1), we can obtain the equations for the first- and second-order expansions in $K$, respectively:

$$\left(\frac{\partial}{\partial t_1} + \boldsymbol{e}_{\alpha} \cdot \boldsymbol{\nabla}_1\right) f_{\alpha}^{eq} + \frac{1}{\tau_f} f_{\alpha}^{(1)} = 0, \tag{8}$$

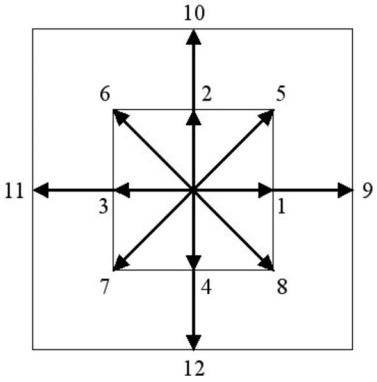


FIG. 1. Discrete velocities of the D2Q12 model.

$$\frac{\partial f_{\alpha}^{eq}}{\partial t_2} + \left(\frac{\partial}{\partial t_1} + \boldsymbol{e}_{\alpha} \cdot \boldsymbol{\nabla}_1\right) f_{\alpha}^{(1)} + \frac{1}{\tau_f} f_{\alpha}^{(2)} = 0. \tag{9}$$

Taking the zeroth- and first-moment summations of Eq. (8), we have

$$\frac{\partial \rho}{\partial t_1} + \boldsymbol{\nabla}_1 \cdot (\rho \boldsymbol{u}) = 0, \tag{10}$$

$$\frac{\partial}{\partial t_1}(\rho u_j) + \frac{\partial}{\partial r_{1i}}(\rho u_i u_j) = -\frac{\partial p}{\partial r_{1j}}. \tag{11}$$

Similarly, taking the summations of Eq. (9), we can obtain the following equations on the $t_2 = K^2 t$ time scale:

$$\frac{\partial \rho}{\partial t_2} = 0, \tag{12}$$

$$\frac{\partial}{\partial t_2}(\rho u_j) + \frac{\partial}{\partial r_{1i}}\left(\sum_{\alpha} e_{\alpha i} e_{\alpha j} f_{\alpha}^{(1)}\right) = 0. \tag{13}$$

With the aid of Eq. (8), $\Sigma_{\alpha} e_{\alpha i} e_{\alpha j} f_{\alpha}^{(1)}$ can be written as

$$\sum_{\alpha} e_{\alpha i} e_{\alpha j} f_{\alpha}^{(1)} = -\tau_f \left[\frac{\partial}{\partial t_1}\left(\sum_{\alpha} e_{\alpha i} e_{\alpha j} f_{\alpha}^{eq}\right) + \frac{\partial}{\partial r_{1k}}\left(\sum_{\alpha} e_{\alpha i} e_{\alpha j} e_{\alpha k} f_{\alpha}^{eq}\right)\right]. \tag{14}$$

Combining Eq. (10) with Eq. (11), after some standard algebra, we can obtain

$$\frac{\partial(\rho u_i u_j)}{\partial t_1} = -u_i \frac{\partial p}{\partial r_{1j}} - u_j \frac{\partial p}{\partial r_{1i}} - \frac{\partial}{\partial r_{1k}}(\rho u_i u_j u_k). \tag{15}$$

Multiplying Eq. (8) by $e_{\alpha}^2$ and summing gives

$$\frac{\partial}{\partial t_1}(\rho u^2 + Dp) + \frac{\partial}{\partial r_{1i}}[\rho u^2 u_i + (D+2)pu_i] = 0. \tag{16}$$

Combining Eq. (16) with Eq. (11), we can obtain

$$\frac{\partial p}{\partial t_1} = -\frac{\partial}{\partial r_{1k}}(pu_k) - \frac{2}{D} p \frac{\partial u_k}{\partial r_{1k}}. \tag{17}$$

With these results, and using Eqs. (3c) and (3d), we can simplify Eq. (14) as

$$\sum_{\alpha} e_{\alpha i} e_{\alpha j} f_{\alpha}^{(1)} = -\tau_f p \left( \frac{\partial u_i}{\partial r_{1j}} + \frac{\partial u_j}{\partial r_{1i}} - \frac{2}{D} \frac{\partial u_k}{\partial r_{1k}} \delta_{ij} \right). \quad (18)$$

Adding Eq. (10) and $K$ times Eq. (12) yields the continuity equation

$$\frac{\partial \rho}{\partial t} + \nabla \cdot (\rho \boldsymbol{u}) = 0. \quad (19)$$

Finally, combining Eqs. (11), (13), and (18), we can obtain the compressible momentum equation

$$\frac{\partial (\rho \boldsymbol{u})}{\partial t} + \nabla \cdot (\rho \boldsymbol{u} \boldsymbol{u}) = -\nabla p + \nabla \cdot \boldsymbol{\Pi}. \quad (20)$$

The viscous stress tensor $\boldsymbol{\Pi}$ is given by

$$\boldsymbol{\Pi} = \mu \left[ \nabla \boldsymbol{u} + (\nabla \boldsymbol{u})^{\mathrm{T}} - \frac{2}{D} (\nabla \cdot \boldsymbol{u}) \mathbf{I} \right], \quad (21)$$

where $\mu = \tau_f p$ is the dynamic viscosity and $\mathbf{I}$ is the unit tensor.

It should be noted that the density distribution function which satisfies Eq. (3) can construct a self-governed lattice Boltzmann model for the compressible continuity and momentum equations, and the pressure is given by Eq. (6). However, in this work, the density distribution function will be used to construct coupled DDF model and the pressure will not be calculated by Eq. (6).

For the D2Q9 model, which is often used in previous DDF models, the pressure $p$ is dependent on the density $\rho$ and calculated by $p(\rho) = \rho c^2/3$ ($c$ is a constant). Consequently, there is no way to couple the two different distribution functions in these DDF models. Moreover, from Eq. (10), the following equation can be obtain:

$$\frac{\partial p(\rho)}{\partial t_1} = -\frac{\partial}{\partial r_{1k}} [p(\rho) u_k]. \quad (22)$$

In addition, Eq. (3d) cannot be completely satisfied because the sixth-rank lattice tensor of the nine-velocity-square lattice is anisotropic. Finally, the momentum equation is given by

$$\frac{\partial (\rho \boldsymbol{u})}{\partial t} + \nabla \cdot (\rho \boldsymbol{u} \boldsymbol{u}) = -\nabla p + \nabla \cdot \{ \mu [\nabla \boldsymbol{u} + (\nabla \boldsymbol{u})^{\mathrm{T}}] - \tau_f \nabla \cdot (\rho \boldsymbol{u} \boldsymbol{u} \boldsymbol{u}) \}. \quad (23)$$

Accordingly, additional particle velocities must be used in order to recover the compressible momentum equation correctly. In this study, a 2-dimensional (2D) 12-velocity (D2Q12) square lattice (see Fig. 1), which can ensure the 6th-rank lattice tensor isotropic, is adopted and defined as

$$\boldsymbol{e}_{\alpha} = \begin{cases} \tilde{c}\{\cos[(\alpha-1)\pi/2], \sin[(\alpha-1)\pi/2]\}, & \alpha = 1,2,3,4, \\ \sqrt{2}\tilde{c}\{\cos[(2\alpha-1)\pi/2], \sin[(2\alpha-1)\pi/2]\}, & \alpha = 5,6,7,8, \\ 2\tilde{c}\{\cos[(\alpha-9)\pi/2], \sin[(\alpha-9)\pi/2]\}, & \alpha = 9,10,11,12, \end{cases} \quad (24)$$

where $\tilde{c} = \sqrt{RT_c}$ ($T_c$ is the characteristic temperature) is the characteristic speed of the lattice fluid. On the other hand, it is well known that, for compressible flows, the continuity equation is taken as the transport equation for the density and the energy equation is the transport equation for the temperature. The pressure is obtained from the density and temperature by using the thermal equation of state, $p = p(\rho, T)$, so we can naturally use the thermal equation of state to couple the two different distribution functions in the DDF models. Details about constructing coupled DDF models will be shown in the next subsection.

### B. Energy distribution functions and coupled DDF models

The first method to construct DDF lattice Boltzmann models was proposed by He *et al.* [14]. This method introduces an internal energy distribution function $g$, which is defined as

$$g = \frac{(\boldsymbol{\xi} - \boldsymbol{u})^2}{2} f, \quad (25)$$

where $\boldsymbol{\xi}$ is the particle velocity. The evolution equations for the continuous density and internal energy distribution functions are given by

$$\frac{\partial f}{\partial t} + (\boldsymbol{\xi} \cdot \nabla) f = -\frac{1}{\tau_f} (f - f^{eq}), \quad (26a)$$

$$\frac{\partial g}{\partial t} + (\boldsymbol{\xi} \cdot \nabla) g = -\frac{1}{\boldsymbol{\tau}_g} (g - g^{eq}) - fq, \quad (26b)$$

where $f^{eq}$ is the Maxwellian equilibrium distribution function, $g^{eq} = (\boldsymbol{\xi} - \boldsymbol{u})^2 f^{eq}/2$ is the equilibrium internal energy distribution function, $\boldsymbol{\tau}_g$ is the relaxation time for the internal energy, and $q$ is given by

$$q = (\boldsymbol{\xi} - \boldsymbol{u}) \cdot \left[ \frac{\partial \boldsymbol{u}}{\partial t} + (\boldsymbol{\xi} \cdot \nabla) \boldsymbol{u} \right]. \quad (27)$$

Note that Eq. (26b) is derived based on the definition of the internal energy distribution function given by Eq. (25). Then the internal energy $\varepsilon$ is defined as $\varepsilon=\int g d\boldsymbol{\xi}=DRT/2$ ($R$ is the specific gas constant), which implies that the macroscopic internal energy only includes the translational kinetic energy. This may be true for monatomic molecules, but polyatomic molecules also possess internal energy associated with the rotational and/or vibrational energy modes. Thus it is necessary to redefine the internal energy distribution function in order to extend the DDF method for polyatomic molecules.

As reported in Refs. [35,18], for polyatomic molecules, the continuous-density distribution function can be expressed by $\tilde{f}=\tilde{f}(\boldsymbol{r},\boldsymbol{\xi},\boldsymbol{\eta},t)$, where $\boldsymbol{\eta}$ is a vector containing $\tilde{K}$ components corresponding to the internal freedom. And the equilibrium density distribution function is given by

$$\tilde{f}^{eq}=\frac{\rho}{2(2\pi RT)^{(D+\tilde{K})/2}}\exp\left[-\frac{(\boldsymbol{\xi}-\boldsymbol{u})^2+\boldsymbol{\eta}^2}{2RT}\right]. \tag{28}$$

Here we introduce a constant $b$, which is related to the specific-heat ratio $\gamma$ by $\gamma=(b+2)/b$, and specify that $(D+\tilde{K})$ is equal to $b$. For the polyatomic molecules, the internal energy distribution function and its equilibrium distribution can be defined as

$$\tilde{g}=\frac{(\boldsymbol{\xi}-\boldsymbol{u})^2+\boldsymbol{\eta}^2}{2}\tilde{f},\quad \tilde{g}^{eq}=\frac{(\boldsymbol{\xi}-\boldsymbol{u})^2+\boldsymbol{\eta}^2}{2}\tilde{f}^{eq}. \tag{29}$$

Since the macroscopic quantities are given by

$$\rho=\int\int\tilde{f}d\boldsymbol{\eta}d\boldsymbol{\xi},\quad \rho\boldsymbol{u}=\int\int\boldsymbol{\xi}\tilde{f}d\boldsymbol{\eta}d\boldsymbol{\xi},\quad \rho\frac{b}{2}RT=\int\int\tilde{g}d\boldsymbol{\eta}d\boldsymbol{\xi}, \tag{30}$$

it is natural to define $\bar{f}=\int\tilde{f}d\boldsymbol{\eta}$ and $\bar{g}=\int\tilde{g}d\boldsymbol{\eta}$, and then the following equations can be obtained:

$$\frac{\partial\bar{f}}{\partial t}+(\boldsymbol{\xi}\cdot\boldsymbol{\nabla})\bar{f}=-\frac{1}{\tau_f}(\bar{f}-\bar{f}^{eq}), \tag{31a}$$

$$\frac{\partial\bar{g}}{\partial t}+(\boldsymbol{\xi}\cdot\boldsymbol{\nabla})\bar{g}=-\frac{1}{\tau_g}(\bar{g}-\bar{g}^{eq})-\bar{f}q, \tag{31b}$$

where

$$\bar{f}^{eq}=\int\tilde{f}^{eq}d\boldsymbol{\eta}=\frac{\rho}{2(2\pi RT)^{D/2}}\exp\left[-\frac{(\boldsymbol{\xi}-\boldsymbol{u})^2}{2RT}\right]=f^{eq}, \tag{32a}$$

$$\bar{g}^{eq}=\int\tilde{g}^{eq}d\boldsymbol{\eta}=\frac{\rho[(\boldsymbol{\xi}-\boldsymbol{u})^2+(b-D)RT]}{2(2\pi RT)^{D/2}}\exp\left[-\frac{(\boldsymbol{\xi}-\boldsymbol{u})^2}{2RT}\right]. \tag{32b}$$

Note that $\int_{-\infty}^{+\infty}\exp(-\varsigma x^2)dx=\sqrt{\pi/\varsigma}$ and $\int_{-\infty}^{+\infty}x^2\exp(-\varsigma x^2)dx=\sqrt{\pi/\varsigma^3}/2$ are used in the derivations. With the above results, we know that Eqs. (26a) and (26b) are also valid for polyatomic molecules as long as the equilibrium distribution functions are chosen appropriately. After some standard algebra, the following equations can be obtained:

$$\int\bar{g}^{eq}d\boldsymbol{\xi}=\rho\frac{b}{2}RT, \tag{33a}$$

$$\int\bar{g}^{eq}\xi_i d\boldsymbol{\xi}=\rho\frac{b}{2}RTu_i, \tag{33b}$$

$$\int\bar{g}^{eq}\xi_i\xi_j d\boldsymbol{\xi}=\rho\frac{b}{2}RTu_iu_j+p\frac{b+2}{2}RT\delta_{ij}. \tag{33c}$$

When the velocity space $\boldsymbol{\xi}$ is discretized into a finite set of velocities $\{\boldsymbol{e}_\alpha\}$, the evolution equation for the discrete internal energy distribution function $g_\alpha$ is given by

$$\frac{\partial g_\alpha}{\partial t}+(\boldsymbol{e}_\alpha\cdot\boldsymbol{\nabla})g_\alpha=-\frac{1}{\tau_g}(g_\alpha-g_\alpha^{eq})-f_\alpha q_\alpha, \tag{34}$$

where $g_\alpha^{eq}$ is the discrete equilibrium internal energy distribution function, which should satisfy the following equations according to Eqs. (33):

$$\sum_\alpha g_\alpha^{eq}=\rho\frac{b}{2}RT, \tag{35a}$$

$$\sum_\alpha e_{\alpha i}g_\alpha^{eq}=\rho\frac{b}{2}RTu_i, \tag{35b}$$

$$\sum_\alpha e_{\alpha i}e_{\alpha j}g_\alpha^{eq}=\rho\frac{b}{2}RTu_iu_j+p\frac{b+2}{2}RT\delta_{ij}. \tag{35c}$$

Through the Chapman-Enskog expansion, we can obtain the macroscopic conservation equation of the internal energy with a flexible specific-heat ratio (see Appendix A for details)

$$\frac{\partial}{\partial t}(\rho c_v T)+\boldsymbol{\nabla}\cdot(\rho c_v T\boldsymbol{u})=\boldsymbol{\nabla}\cdot(\lambda\boldsymbol{\nabla}T)+\boldsymbol{\Pi}':\boldsymbol{\nabla}\boldsymbol{u}-p\boldsymbol{\nabla}\cdot\boldsymbol{u}, \tag{36}$$

where $c_v=bR/2$ is the specific heat at constant volume and $\lambda=\tau_g(c_v+R)p$ is the thermal conductivity. The pressure is

calculated by the thermal equation of state, such as $p=\rho RT$ for an ideal gas. At this point, it should be noted that Eq. (7) together with Eq. (16) is invalid because the pressure is not defined by Eq. (6). This change affects the form of the viscous stress tensor, which now is given by

$$\mathbf{\Pi}' = \mu\left[\nabla\boldsymbol{u} + (\nabla\boldsymbol{u})^{\mathrm{T}} - \frac{2}{D}(\nabla\cdot\boldsymbol{u})\mathbf{I}\right] + \mu_B(\nabla\cdot\boldsymbol{u})\mathbf{I}, \quad (37)$$

where $\mu_B=2(1/D-1/b)\tau_f p$ is the bulk viscosity.

Recently, Guo *et al.* [18] proposed another method to construct DDF models by introducing a total energy distribution function $h=\boldsymbol{\xi}^2 f/2$, and its evolution equation is given as follows:

$$\frac{\partial h}{\partial t} + (\boldsymbol{\xi}\cdot\nabla)h = -\frac{1}{\tau_h}(h-h^{eq}) + \frac{1}{\tau_{hf}}\left(\boldsymbol{\xi}\cdot\boldsymbol{u} - \frac{u^2}{2}\right)(f-f^{eq}), \quad (38)$$

where $h^{eq}$ is the equilibrium total energy distribution function, $\tau_h$ is the total energy relaxation time, and $\tau_{hf}=\tau_h\tau_f/(\tau_f-\tau_h)$.

Similarly, although Eq. (38) is derived based on $h=\boldsymbol{\xi}^2 f/2$, this method can also be extended for polyatomic molecules with the corresponding equilibrium total energy distribution function given by

$$h^{eq} = \frac{\rho[\boldsymbol{\xi}^2 + (b-D)RT]}{2(2\pi RT)^{D/2}}\exp\left[-\frac{(\boldsymbol{\xi}-\boldsymbol{u})^2}{2RT}\right]. \quad (39)$$

Up to now, we have shown that both methods can be extended to construct DDF models for the compressible NS equations with arbitrary specific-heat ratio (adjusted by the constant $b$) by selecting appropriate forms of equilibrium distribution functions. Considering the simplicity of the latter method, we adopt the total energy distribution function for numerical simulations in this study, and the following evolution equation is presented:

$$\frac{\partial h_\alpha}{\partial t} + (\boldsymbol{e}_\alpha\cdot\nabla)h_\alpha = -\frac{1}{\tau_h}(h_\alpha - h_\alpha^{eq}) + \frac{1}{\tau_{hf}}(\boldsymbol{e}_\alpha\cdot\boldsymbol{u})(f_\alpha - f_\alpha^{eq}). \quad (40)$$

The simplification from $(\boldsymbol{e}_\alpha\cdot\boldsymbol{u}-u^2/2)$ to $(\boldsymbol{e}_\alpha\cdot\boldsymbol{u})$ does not affect the form of the compressible energy equation at the Naiver-Stokes level, which can be seen clearly in Appendix B.

The equilibrium total energy distribution should satisfy the following velocity moment condition:

$$\sum_\alpha h_\alpha^{eq} = \rho E, \quad (41a)$$

$$\sum_\alpha e_{\alpha i} h_\alpha^{eq} = (\rho E + p)u_i, \quad (41b)$$

$$\sum_\alpha e_{\alpha i} e_{\alpha j} h_\alpha^{eq} = (\rho E + 2p)u_i u_j + p(E+RT)\delta_{ij}, \quad (41c)$$

where $E=bRT/2+u^2/2$ is the total energy. Then the temperature is calculated by

$$T = \frac{2}{bR}\left(\sum_\alpha h_\alpha - \frac{u^2}{2}\right). \quad (42)$$

Through the Chapman-Enskog expansion, we can obtain the compressible energy equation (see Appendix B for details)

$$\frac{\partial}{\partial t}(\rho E) + \nabla\cdot[(\rho E + p)\boldsymbol{u}] = \nabla\cdot(\lambda\nabla T) + \nabla\cdot(\boldsymbol{u}\cdot\mathbf{\Pi}'), \quad (43)$$

where $\lambda=\tau_h(c_v+R)p$. The viscous stress tensor $\Pi'$ is given by Eq. (37), and the momentum equation is given as follows:

$$\frac{\partial(\rho\boldsymbol{u})}{\partial t} + \nabla\cdot(\rho\boldsymbol{u}\boldsymbol{u}) = -\nabla p + \nabla\cdot\mathbf{\Pi}'. \quad (44)$$

The Prandtl number of the system, $\mathrm{Pr}=\mu c_p/\lambda=\tau_f/\tau_h$, can be made arbitrary by adjusting the two relaxation times.

In the following, we will specify the detailed forms of the equilibrium distribution functions. Taking the equilibrium density distribution function as an example, it can be determined by several methods. The first method, which is the conventional method, is based on the discrete Maxwellian equilibrium distribution function

$$f_\alpha^{eq} = \frac{\rho}{(2\pi RT)^{D/2}}\exp\left(-\frac{(\boldsymbol{e}_\alpha-\boldsymbol{u})^2}{2RT}\right). \quad (45)$$

Owing to the finite number of discrete velocities, Eq. (45) cannot fulfill the conservation laws and the constraints to recover the macroscopic equations. Thus, the truncated Maxwellian equilibrium distribution with an expansion in powers of local velocity $\boldsymbol{u}$ is used to replace Eq. (45). This method is widely used in the current LBM community for it is easy to be accepted and implemented. Its disadvantage is that it is limited to low- and moderate-Mach-number flows. The second method has nothing to do with the Maxwellian equilibrium distribution. In this method, the equilibrium distribution function can be a Kronecker $\delta$ function [24–28] or a circular function [22], and the former, as pointed out in Ref. [4], is in fact related to the beam scheme. The connections and differences between the LBM and the beam scheme can be found in Ref. [36]. The main advantage of the second method is that it can be used to simulate high-Mach-number flows.

In this study, we will apply the above two methods to design coupled DDF models. First, the conventional method is used. Note that $f_\alpha^{eq}$ should be expanded up to $u^3$ to satisfy Eq. (3), while $h_\alpha^{eq}$ can only be expanded up to $u^2$. We thus define

$$f_\alpha^{eq} = A_\alpha + B_\alpha(\boldsymbol{e}_\alpha\cdot\boldsymbol{u}) + C_\alpha u^2 + D_\alpha(\boldsymbol{e}_\alpha\cdot\boldsymbol{u})^2 + G_\alpha(\boldsymbol{e}_\alpha\cdot\boldsymbol{u})u^2 + H_\alpha(\boldsymbol{e}_\alpha\cdot\boldsymbol{u})^3, \quad (46)$$

$$h_\alpha^{eq} = K_\alpha + L_\alpha(\boldsymbol{e}_\alpha\cdot\boldsymbol{u}) + M_\alpha u^2 + N_\alpha(\boldsymbol{e}_\alpha\cdot\boldsymbol{u})^2. \quad (47)$$

The coefficients $A_\alpha,\ldots,H_\alpha,K_\alpha,\ldots,N_\alpha$ can be obtained by solving the corresponding constraints. As some of these constraints are underconditioned, the solutions are somewhat arbitrary. For the D2Q12 square lattice, one possible solution for $f_\alpha^{eq}$ and $h_\alpha^{eq}$ is given as follows:

$$f_{1,2,3,4}^{eq}=\rho\left[\frac{1}{12}\left(5-\frac{4p}{\rho\tilde{c}^2}\right)+\left(2-\frac{3p}{\rho\tilde{c}^2}\right)\frac{(\boldsymbol{e}_\alpha\cdot\boldsymbol{u})}{3\tilde{c}^2}-\frac{u^2}{6\tilde{c}^2}+\frac{(\boldsymbol{e}_\alpha\cdot\boldsymbol{u})^2}{6\tilde{c}^4}-\frac{(\boldsymbol{e}_\alpha\cdot\boldsymbol{u})u^2}{2\tilde{c}^4}+\frac{(\boldsymbol{e}_\alpha\cdot\boldsymbol{u})^3}{3\tilde{c}^6}\right],$$

$$f_{5,6,7,8}^{eq}=\rho\left[\frac{1}{8}\left(\frac{2p}{\rho\tilde{c}^2}-1\right)+\frac{p}{\rho\tilde{c}^2}\frac{(\boldsymbol{e}_\alpha\cdot\boldsymbol{u})}{4\tilde{c}^2}-\frac{u^2}{8\tilde{c}^2}+\frac{(\boldsymbol{e}_\alpha\cdot\boldsymbol{u})^2}{8\tilde{c}^4}-\frac{(\boldsymbol{e}_\alpha\cdot\boldsymbol{u})u^2}{8\tilde{c}^4}+\frac{(\boldsymbol{e}_\alpha\cdot\boldsymbol{u})^3}{8\tilde{c}_6}\right],$$

$$f_{9,10,11,12}^{eq}=\rho\left[\frac{1}{24}\left(\frac{2p}{\rho\tilde{c}^2}-1\right)+\left(\frac{3p}{\rho\tilde{c}^2}-1\right)\frac{(\boldsymbol{e}_\alpha\cdot\boldsymbol{u})}{24\tilde{c}^2}+\frac{u^2}{24\tilde{c}^2}+\frac{(\boldsymbol{e}_\alpha\cdot\boldsymbol{u})^2}{48\tilde{c}^4}+\frac{(\boldsymbol{e}_\alpha\cdot\boldsymbol{u})^3}{96\tilde{c}^6}\right], \tag{48}$$

$$h_{1,2,3,4}^{eq}=\frac{5\rho E}{12}-\frac{p}{3\tilde{c}^2}(E+RT)+\frac{1}{6}\left\{(\rho E+p)\frac{(\boldsymbol{e}_\alpha\cdot\boldsymbol{u})}{\tilde{c}^2}+(\rho E+2p)\left[\frac{(\boldsymbol{e}_\alpha\cdot\boldsymbol{u})^2}{\tilde{c}^4}-\frac{u^2}{\tilde{c}^2}\right]\right\},$$

$$h_{5,6,7,8}^{eq}=-\frac{\rho E}{8}+\frac{p}{4\tilde{c}^2}(E+RT)+\frac{1}{8}\left\{(\rho E+p)\frac{(\boldsymbol{e}_\alpha\cdot\boldsymbol{u})}{\tilde{c}^2}+(\rho E+2p)\left[\frac{(\boldsymbol{e}_\alpha\cdot\boldsymbol{u})^2}{\tilde{c}^4}-\frac{u^2}{\tilde{c}^2}\right]\right\},$$

$$h_{9,10,11,12}^{eq}=-\frac{\rho E}{24}+\frac{p}{12\tilde{c}^2}(E+RT)+\frac{1}{48}\left\{(\rho E+p)\frac{(\boldsymbol{e}_\alpha\cdot\boldsymbol{u})}{\tilde{c}^2}+(\rho E+2p)\left[\frac{(\boldsymbol{e}_\alpha\cdot\boldsymbol{u})^2}{\tilde{c}^4}+2\frac{u^2}{\tilde{c}^2}\right]\right\}. \tag{49}$$

As can be seen in Eq. (48), unlike decoupling DDF models, the pressure term $p=p(\rho,T)$ serves as an independent variable appearing in the equilibrium density distribution function. This means that the equilibrium density distribution function depends on the local temperature $[T=2(\Sigma_\alpha h_\alpha-u^2/2)/bR]$ and provides an implicit coupling between the density distribution function and the total energy distribution function. Thus, the two distribution functions are coupled together by using the thermal equation of state. In addition, from Eq. (49) it can be found that the constant $b$ is introduced to adjust the specific-heat ratio with $E=(bRT+u^2)/2$. Compared with the multispeed thermal models based on a single distribution function, although the present model has an obvious weak point that the computational time needed will be increased because two distribution functions are used, it has an advantage of simplicity and can easily handle arbitrary values of the specific-heat ratio and Prandtl number. In the following, we will use model I to represent Eqs. (1), (40), (48), and (49).

As we have mentioned before, the truncated Maxwellian equilibrium distribution function is limited to low- and moderate-Mach-number flows, which has been validated by much research [8–11]. This limitation mainly results from the Taylor series expansion in terms of the Mach number. Another reason may be that the equilibrium distribution functions determined by this approach contain many free parameters [9,11]. To get satisfied simulation results at high Mach number, these parameters should be tuned carefully. Unfortunately, how to tune these parameters is not clear. Most recently, Qu *et al.* [22] proposed a lattice Boltzmann model for the compressible Euler equations at high Mach number. In this model, a circular function is introduced to replace the Maxwellian equilibrium distribution function, and the circular function is then distributed to the lattice velocity directions by Lagrangian interpolation. An important feature of this model is that it has no free parameters. Therefore, in this study, we adopt the circular function for high-Mach-number flows. However, much work should be done to construct a coupled DDF model for the compressible Navier-Stokes at high Mach number. This is because the model and the equilibrium density distribution function in Ref. [22] are both designed for the compressible Euler equations and the Prandtl number is equal to the specific-heat ratio in their method.

First, we discard the energy level method used in Ref. [22], and the equilibrium density distribution function is then defined as

$$f_\alpha^{eq}=\rho_\alpha, \tag{50}$$

where $\alpha=0,1,2,\ldots,12$ because the D2Q13 square lattice (one more velocity with modulus 0 compared with the D2Q12 square lattice) was used in Ref. [22]. The equilibrium density distribution function of the Euler model devised by Qu *et al.* was given in the Appendix of Ref. [22]. Nevertheless, some changes should be made for the expression before it is introduced as the equilibrium density distribution function of our coupled DDF model. The variable $c$ used there should be replaced by $\sqrt{2p/\rho\tilde{c}^2}$; moreover, $u$ and $v$ (corresponding to $u_x$ and $u_y$ in this paper) are made dimensionless through dividing by $\tilde{c}$, while $\rho$ is dimensional. Then the equilibrium density distribution function is given by

$$\rho_0=\rho/4[\bar{u}_x^4+5\bar{p}^2-10\bar{p}+4+4\bar{u}_x^2\bar{u}_y^2+\bar{u}_y^4+(10\bar{p}-5)(\bar{u}_x^2+\bar{u}_y^2)],$$

$$\rho_1=-\rho/6(-4\bar{u}_x^2+3\bar{p}^2+\bar{u}_x^4-4\bar{p}+3\bar{p}\bar{u}_y^2+3\bar{u}_x\bar{u}_y^2+9\bar{p}\bar{u}_x^2+6\bar{p}\bar{u}_x+3\bar{u}_x^2\bar{u}_y^2-4\bar{u}_x+\bar{u}_x^3),$$

$$\rho_2=-\rho/6(-4\bar{u}_y^2+3\bar{p}^2+\bar{u}_y^4-4\bar{p}+3\bar{p}\bar{u}_x^2+3\bar{u}_x^2\bar{u}_y+9\bar{p}\bar{u}_y^2+6\bar{p}\bar{u}_y+3\bar{u}_x^2\bar{u}_y^2-4\bar{u}_y+\bar{u}_y^3),$$

$$\rho_3=-\rho/6(-4\bar{u}_x^2+3\bar{p}^2+\bar{u}_x^4-4\bar{p}+3\bar{p}\bar{u}_y^2-3\bar{u}_x\bar{u}_y^2+9\bar{p}\bar{u}_x^2-6\bar{p}\bar{u}_x+3\bar{u}_x^2\bar{u}_y^2+4\bar{u}_x-\bar{u}_x^3),$$

$$\rho_4=-\rho/6(-4\bar{u}_y^2+3\bar{p}^2+\bar{u}_y^4-4\bar{p}+3\bar{p}\bar{u}_x^2-3\bar{u}_x^2\bar{u}_y+9\bar{p}\bar{u}_y^2-6\bar{p}\bar{u}_y+3\bar{u}_x^2\bar{u}_y^2+4\bar{u}_y-\bar{u}_y^3),$$

$$\rho_5 = \rho/8(\bar{u}_x\bar{u}_y^2 + \bar{u}_x\bar{u}_y + \bar{p}\bar{u}_x + \bar{p}\bar{u}_y + \bar{u}_x^2\bar{u}_y + 0.5\bar{p}^2 + \bar{u}_x^2\bar{u}_y^2 + \bar{p}\bar{u}_x^2 + \bar{p}\bar{u}_y^2),$$

$$\rho_6 = \rho/8(-\bar{u}_x\bar{u}_y^2 - \bar{u}_x\bar{u}_y - \bar{p}\bar{u}_x + \bar{p}\bar{u}_y + \bar{u}_x^2\bar{u}_y + 0.5\bar{p}^2 + \bar{u}_x^2\bar{u}_y^2 + \bar{p}\bar{u}_x^2 + \bar{p}\bar{u}_y^2),$$

$$\rho_7 = \rho/8(-\bar{u}_x\bar{u}_y^2 + \bar{u}_x\bar{u}_y - \bar{p}\bar{u}_x - \bar{p}\bar{u}_y - \bar{u}_x^2\bar{u}_y + 0.5\bar{p}^2 + \bar{u}_x^2\bar{u}_y^2 + \bar{p}\bar{u}_x^2 + \bar{p}\bar{u}_y^2),$$

$$\rho_8 = \rho/8(\bar{u}_x\bar{u}_y^2 - \bar{u}_x\bar{u}_y + \bar{p}\bar{u}_x - \bar{p}\bar{u}_y - \bar{u}_x^2\bar{u}_y + 0.5\bar{p}^2 + \bar{u}_x^2\bar{u}_y^2 + \bar{p}\bar{u}_x^2 + \bar{p}\bar{u}_y^2),$$

$$\rho_9 = \rho/24(-2\bar{u}_x + \bar{u}_x^4 - \bar{p} - \bar{u}_x^2 + 6\bar{p}\bar{u}_x^2 + 1.5\bar{p}^2 + 2\bar{u}_x^3 + 6\bar{p}\bar{u}_x),$$

$$\rho_{10} = \rho/24(-2\bar{u}_y + \bar{u}_y^4 - \bar{p} - \bar{u}_y^2 + 6\bar{p}\bar{u}_y^2 + 1.5\bar{p}^2 + 2\bar{u}_y^3 + 6\bar{p}\bar{u}_y),$$

$$\rho_{11} = \rho/24(2\bar{u}_x + \bar{u}_x^4 - \bar{p} - \bar{u}_x^2 + 6\bar{p}\bar{u}_x^2 + 1.5\bar{p}^2 - 2\bar{u}_x^3 - 6\bar{p}\bar{u}_x),$$

$$\rho_{12} = \rho/24(2\bar{u}_y + \bar{u}_y^4 - \bar{p} - \bar{u}_y^2 + 6\bar{p}\bar{u}_y^2 + 1.5\bar{p}^2 - 2\bar{u}_y^3 - 6\bar{p}\bar{u}_y). \tag{51}$$

Note that $\bar{p}=p/\rho\tilde{c}^2$, while $\bar{u}_x$ and $\bar{u}_y$ are the dimensionless forms of $u_x$ and $u_y$.

With the above modifications, we can prove that the equilibrium density distribution function given by Eqs. (50) and (51) can satisfy Eq. (3) completely (in the 2D case). However, if we still follow the approach proposed in Ref. [22] to construct the equilibrium total energy distribution function, it will make the equilibrium total energy distribution function very complicated and the following equation will be obtained [compared with Eq. (31) in Ref. [22]]:

$$\sum_\alpha e_{\alpha i}e_{\alpha j}h_\alpha^{eq} = (\rho E + 2p)u_iu_j + pE\delta_{ij} = \frac{1}{2}\{[\rho(b+4)RT + \rho u^2]u_iu_j + \rho(bR^2T^2 + u^2RT)\delta_{ij}\}. \tag{52}$$

By comparing Eq. (52) with Eq. (41c), it can be found that Eq. (52) has a difference from Eq. (41c). As a result, the macroscopic energy equation at the Navier-Stokes level will become

$$\frac{\partial}{\partial t}(\rho E) + \nabla\cdot[(\rho E + p)\boldsymbol{u}] = \nabla\cdot(\lambda\nabla T) + \nabla\cdot(\boldsymbol{u}\cdot\boldsymbol{\Pi}') - \nabla\cdot(\tau_h RT\nabla p), \tag{53}$$

where $\lambda$ now is given by $\lambda=\tau_h c_v p$.

In order to overcome these drawbacks, we propose a simple and general method to determine the equilibrium total energy distribution function as follows (see Appendix C for details):

$$h_\alpha^{eq} = [E + (\boldsymbol{e}_\alpha - \boldsymbol{u})\cdot\boldsymbol{u}]f_\alpha^{eq} + \varpi_\alpha\frac{p}{\tilde{c}^2}RT, \tag{54}$$

where $\varpi_\alpha$ can be obtained by solving Eq. (41) and $\varpi_0=0$, $\varpi_{1,2,3,4}=-1/3$, $\varpi_{5,6,7,8}=1/4$, and $\varpi_{9,10,11,12}=1/12$ are chosen in the present work. By using Eq. (54), the equilibrium total energy distribution function which satisfies Eq. (41) can be very easily derived from its corresponding equilibrium density distribution function; thus, it is not necessary to design a very complicated one. Finally, Eqs. (1), (40), (50), (51), and (54) constitute model II, which can be used to simulate high-Mach-number flows.

## III. NUMERICAL FORMULATION

### A. Time discretization

To solve Eqs. (1) and (40) numerically, we adopt IMEX Runge-Kutta schemes [29–31] which consist of an implicit time discretization for the relaxation term and an explicit one for the other terms. This is because with the high performance of the IMEX Runge-Kutta schemes, we can choose a moderate Courant-Friedriche-Lewy (CFL) number and the accuracy in time can be improved.

To advance the distribution function $f_\alpha$ from time $t$ to $t+\Delta t$ by the IMEX Runge-Kutta schemes, the following computations are conducted:

$$f_\alpha^{\langle m\rangle} = f_\alpha^t - \Delta t\sum_{n=1}^{m-1}\tilde{a}_{mn}(\boldsymbol{e}_\alpha\cdot\nabla f_\alpha^{\langle n\rangle}) + \Delta t\sum_{n=1}^{m}a_{mn}\frac{f_\alpha^{eq\langle n\rangle} - f_\alpha^{\langle n\rangle}}{\tau_f^{\langle n\rangle}}, \tag{55}$$

$$f_\alpha^{t+\Delta t} = f_\alpha^t - \Delta t\sum_{m=1}^{l}\tilde{w}_m(\boldsymbol{e}_\alpha\cdot\nabla f_\alpha^{\langle m\rangle}) + \Delta t\sum_{m=1}^{l}w_m\frac{f_\alpha^{eq\langle m\rangle} - f_\alpha^{\langle m\rangle}}{\tau_f^{\langle m\rangle}}, \tag{56}$$

where $f_\alpha^{\langle m\rangle}$, $f_\alpha^{eq\langle m\rangle}$, $\tau_f^{\langle m\rangle}$, and $l$ are the $m$th stage density distribution function, local equilibrium distribution function, relaxation time, and total stage number, respectively. The two $l\times l$ matrices $\tilde{\boldsymbol{a}}=(\tilde{a}_{mn})$ ($\tilde{a}_{mn}=0$ for $n\geqslant m$) and $\boldsymbol{a}=(a_{mn})$ ($a_{mn}=0$ for $n>m$) and the two vectors $\tilde{\boldsymbol{w}}=(\tilde{w}_1,\ldots,\tilde{w}_l)^T$ and $\boldsymbol{w}=(w_1,\ldots,w_l)^T$ characterize the IMEX Runge-Kutta schemes. Equations (55) and (56) are, respectively, the implicit and explicit parts of the schemes. Similarly, the following equations can be obtained for $h_\alpha$:

$$h_\alpha^{\langle m\rangle} = h_\alpha^t - \Delta t\sum_{n=1}^{m-1}\tilde{a}_{mn}(\boldsymbol{e}_\alpha\cdot\nabla h_\alpha^{\langle n\rangle}) + \Delta t\sum_{n=1}^{m}a_{mn}\frac{h_\alpha^{eq\langle n\rangle} - h_\alpha^{\langle n\rangle}}{\tau_h^{\langle n\rangle}} - \Delta t\sum_{n=1}^{m}a_{mn}(\boldsymbol{e}_\alpha\cdot\boldsymbol{u}^{\langle n\rangle})\frac{f_\alpha^{eq\langle n\rangle} - f_\alpha^{\langle n\rangle}}{\tau_{hf}^{\langle n\rangle}}, \tag{57}$$

$$h_\alpha^{t+\Delta t} = h_\alpha^t - \Delta t\sum_{m=1}^{l}\tilde{w}_m(\boldsymbol{e}_\alpha\cdot\nabla h_\alpha^{\langle m\rangle}) + \Delta t\sum_{m=1}^{l}w_m\frac{h_\alpha^{eq\langle m\rangle} - h_\alpha^{\langle m\rangle}}{\tau_h^{\langle m\rangle}} - \Delta t\sum_{m=1}^{l}w_m(\boldsymbol{e}_\alpha\cdot\boldsymbol{u}^{\langle m\rangle})\frac{f_\alpha^{eq\langle m\rangle} - f_\alpha^{\langle m\rangle}}{\tau_{hf}^{\langle m\rangle}}. \tag{58}$$

For the implicit of Eq. (55), it is natural to adopt diagonally implicit Runge-Kutta schemes for the relaxation term [29]. This will be an arduous procedure because not only $f_\alpha^{\langle m\rangle}$ but also $f_\alpha^{eq\langle m\rangle}$ are needed to be fixed in iteration. Fortunately, the characteristic of the collision invariants of $f_\alpha$, $\varphi=(1,\mathbf{e}_\alpha)^{\mathrm{T}}$, brings us a simple trick to update $f_\alpha^{\langle m\rangle}$ without iteration. For $f_\alpha^{\langle m\rangle}$, we rewrite Eq. (55) as

$$\sum_\alpha f_\alpha^{\langle m\rangle}\varphi=\sum_\alpha f_\alpha^t\varphi-\Delta t\sum_{n=1}^{m-1}\tilde{a}_{mn}\left[\sum_\alpha(\boldsymbol{e}_\alpha\cdot\nabla f_\alpha^{\langle n\rangle})\varphi\right]+\Delta t\sum_{n=1}^{m}\frac{a_{mn}}{\tau_f^{\langle n\rangle}}\left[\sum_\alpha(f_\alpha^{eq\langle n\rangle}-f_\alpha^{\langle n\rangle})\varphi\right], \tag{59}$$

and noting that $\Sigma_\alpha[(f_\alpha^{eq\langle n\rangle}-f_\alpha^{\langle n\rangle})\varphi]=0$, we can obtain

$$\sum_\alpha f_\alpha^{\langle m\rangle}\varphi=\sum_\alpha f_\alpha^t\varphi-\Delta t\sum_{n=1}^{m-1}\tilde{a}_{mn}\left[\sum_\alpha(\boldsymbol{e}_\alpha\cdot\nabla f_\alpha^{\langle n\rangle})\varphi\right]. \tag{60}$$

Similarly, for $h_\alpha^{\langle m\rangle}$, we have

$$\sum_\alpha h_\alpha^{\langle m\rangle}=\sum_\alpha h_\alpha^t-\Delta t\sum_{n=1}^{m-1}\tilde{a}_{mn}\left[\sum_\alpha(\boldsymbol{e}_\alpha\cdot\nabla h_\alpha^{\langle n\rangle})\right]. \tag{61}$$

Equations (60) and (61) mean the $m$th-stage macroscopic variables $(\rho^{\langle m\rangle},\boldsymbol{u}^{\langle m\rangle},T^{\langle m\rangle},p^{\langle m\rangle})$ can be calculated explicitly from the previous stages. With these stage variables, we can update the corresponding equilibrium distribution functions and the relaxation times. As a result, $f_\alpha^{\langle m\rangle}$ and $h_\alpha^{\langle m\rangle}$ can be explicitly given by

$$f_\alpha^{\langle m\rangle}=\frac{f_\alpha^t-\Delta t\sum_{n=1}^{m-1}\tilde{a}_{mn}(\boldsymbol{e}_\alpha\cdot\nabla f_\alpha^{\langle n\rangle})+\Delta t\sum_{n=1}^{m-1}a_{mn}\frac{f_\alpha^{eq\langle n\rangle}-f_\alpha^{\langle n\rangle}}{\tau_f^{\langle n\rangle}}+\frac{\Delta t}{\tau_f^{\langle m\rangle}}a_{mm}f_\alpha^{eq\langle m\rangle}}{1+\frac{\Delta t}{\tau_f^{\langle m\rangle}}a_{mm}}, \tag{62}$$

$$h_\alpha^{\langle m\rangle}=\frac{h_\alpha^t-\Delta t\sum_{n=1}^{m-1}\tilde{a}_{mn}(\boldsymbol{e}_\alpha\cdot\nabla h_\alpha^{\langle n\rangle})-\Delta t\sum_{n=1}^{m}a_{mn}(\boldsymbol{e}_\alpha\cdot\boldsymbol{u}^{\langle n\rangle})\frac{f_\alpha^{eq\langle n\rangle}-f_\alpha^{\langle n\rangle}}{\tau_{hf}^{\langle n\rangle}}+\Delta t\sum_{n=1}^{m-1}a_{mn}\frac{h_\alpha^{eq\langle n\rangle}-h_\alpha^{\langle n\rangle}}{\tau_h^{\langle n\rangle}}+\frac{\Delta t}{\tau_h^{\langle m\rangle}}a_{mm}h_\alpha^{eq\langle m\rangle}}{1+\frac{\Delta t}{\tau_h^{\langle m\rangle}}a_{mm}}. \tag{63}$$

In summary, Eqs. (56) and (62) can be regarded as the governing equations of the IMEX Runge-Kutta schemes for the density distribution function, while Eqs. (58) and (63) are the governing equations for the total energy distribution function. Note that implicitness is completely eliminated, although the IMEX scheme is used.

It is required that, to enhance the computational accuracy, the coefficients $\tilde{a}_{mn}$, $a_{mn}$, $\tilde{w}_m$, and $w_m$ should be determined in order. The coefficients of the second-order and third-order IMEX Runge-Kutta schemes [29,30] are given in Appendix D.

### B. Space discretization

In this work, the fifth-order weighted essentially nonoscillatory (WENO) scheme [30,32] and the total variation diminishing (TVD) scheme [22] are adopted to capture the discontinuities in the compressible flows. The WENO scheme is an improvement on the essentially nonoscillatory (ENO) scheme, and it uses a convex combination of all candidate stencils instead of just one as in the original ENO scheme. A high-resolution scheme of space discretization is necessary to capture the discontinuities and shock waves well. For the 2D flows, in consideration of the $x$ component of the convection term $\boldsymbol{e}_\alpha\cdot\nabla f_\alpha$ in Eqs. (56) and (62), we give the details of this scheme:

$$\frac{\partial(\boldsymbol{e}_{\alpha x}f_\alpha)}{\partial x}=\frac{1}{\Delta x}(\hat{F}_{\alpha,I+1/2,J}-\hat{F}_{\alpha,I-1/2,J}), \tag{64}$$

where $e_{\alpha x}$ is the $x$ component of $\boldsymbol{e}_\alpha$; $\hat{F}_{\alpha,I+1/2,J}$ is the numerical flux at the interface of $x_I+\Delta x/2$ ($I$ and $J$ are node indexes), and it is defined as

$$\hat{F}_{\alpha,I+1/2,J}=\omega_1\hat{F}^1_{\alpha,I+1/2,J}+\omega_2\hat{F}^2_{\alpha,I+1/2,J}+\omega_1\hat{F}^3_{\alpha,I+1/2,J}. \tag{65}$$

Under the condition $e_{\alpha x}\geqslant 0$, three third-order fluxes on three different stencils are given by

$$\hat{F}^1_{\alpha,I+1/2,J}=\frac{1}{3}F_{\alpha,I-2,J}-\frac{7}{6}F_{\alpha,I-1,J}+\frac{11}{6}F_{\alpha,I,J}, \tag{66a}$$

$$\hat{F}^2_{\alpha,I+1/2,J}=-\frac{1}{6}F_{\alpha,I-1,J}+\frac{5}{6}F_{\alpha,I,J}+\frac{1}{3}F_{\alpha,I+1,J}, \tag{66b}$$

$$\hat{F}^3_{\alpha,I+1/2,J}=\frac{1}{3}F_{\alpha,I,J}+\frac{5}{6}F_{\alpha,I+1,J}-\frac{1}{6}F_{\alpha,I+2,J}, \tag{66c}$$

where $F_{\alpha,I,J}=e_{\alpha x}f_{\alpha,I,J}$.

The weighting factors $\omega_q$ in Eq. (65) are given by

$$\omega_q = \frac{\tilde{\omega}_q}{\tilde{\omega}_1 + \tilde{\omega}_2 + \tilde{\omega}_3}, \quad \tilde{\omega}_q = \frac{\delta_q}{(10^{-6} + \sigma_q)^2}, \tag{67}$$

with $\delta_1 = 1/10$, $\delta_2 = 3/5$, and $\delta_3 = 3/10$. The small value $10^{-6}$ is added to the denominator to avoid dividing by zero. The coefficients $\sigma_q$ in Eq. (67) are the smoothness indicators and can be obtained by

$$\sigma_1 = \frac{13}{12}(F_{\alpha,I-2,J} - 2F_{\alpha,I-1,J} + F_{\alpha,I,J})^2 + \frac{1}{4}(F_{\alpha,I-2,J} - 4F_{\alpha,I-1,J} + 3F_{\alpha,I,J})^2, \tag{68a}$$

$$\sigma_2 = \frac{13}{12}(F_{\alpha,I-1,J} - 2F_{\alpha,I,J} + F_{\alpha,I+1,J})^2 + \frac{1}{4}(F_{\alpha,I-1,J} - F_{\alpha,I+1,J})^2, \tag{68b}$$

$$\sigma_3 = \frac{13}{12}(F_{\alpha,I,J} - 2F_{\alpha,I+1,J} + F_{\alpha,I+2,J})^2 + \frac{1}{4}(3F_{\alpha,I,J} - 4F_{\alpha,I+1,J} + F_{\alpha,I+2,J})^2. \tag{68c}$$

Similarly, under the condition $e_{\alpha x} < 0$, a mirror image procedure (with respect to $I+1/2$) of the procedure from Eqs. (65)–(68) can be carried out. For 2D problems, these scheme should be applied in both the $x$ and $y$ directions.

Finally, it should be pointed out that the Euler and second-upwind-difference schemes can also be used when the flows do not have shock waves or discontinuities, and the distribution functions of next step are calculated by

$$f_\alpha^{t+\Delta t} = f_\alpha^t - \Delta t(\boldsymbol{e}_\alpha \cdot \nabla f_\alpha^t) + \Delta t \frac{f_\alpha^{eq,t} - f_\alpha^t}{\tau_f^t}, \tag{69}$$

$$h_\alpha^{t+\Delta t} = h_\alpha^t - \Delta t(\boldsymbol{e}_\alpha \cdot \nabla h_\alpha^t) + \Delta t \frac{h_\alpha^{eq,t} - h_\alpha^t}{\tau_h^t} - \Delta t(\boldsymbol{e}_\alpha \cdot \boldsymbol{u}^t)\frac{f_\alpha^{eq,t} - f_\alpha^t}{\tau_{hf}^t}, \tag{70}$$

where $\nabla f_\alpha^t$ and $\nabla h_\alpha^t$ are calculated by using the second upwind difference. Note that the Euler scheme only has first-order accuracy in time.

## IV. NUMERICAL TESTS

In Sec. II, we have developed a coupled DDF lattice Boltzmann method with a flexible specific-heat ratio and Prandtl number for the compressible NS equations, and two 2D coupled DDF models have also been designed there. In this section, as preliminary tests, numerical simulations are performed for the Riemann problem, the double-Mach-reflection problem, and the Couette flow to validate these models. The reference density $\rho_0$ and the reference temperature $T_0$ are used in simulations, and the reference velocity and the reference pressure are defined as $u_0 = \sqrt{RT_0}$, $p_0 = \rho_0 R T_0$. The characteristic temperature $T_c$ is often set to a value which is a little bit larger than the maximum stagnation temperature in the whole flow field, $T_c \geqslant \max(T^*)$ where $T^* = T[1 + (\gamma - 1)Ma^2/2]$.

### A. Riemann problem

The flow of the Riemann problem includes a shock wave, a contact surface, and an expansion wave; hence, it makes a wonderful model problem on which to study the performance of the numerical schemes in simulation of compressible flows. Two different cases are considered in this study.

*Case 1.* Sod shock-tube with the initial condition as follows:

$$(\rho/\rho_0, u_x/u_0, p/p_0) = (1,0,1), \quad 0 < x/L_0 \leqslant 1/2,$$

$$(\rho/\rho_0, u_x/u_0, p/p_0) = (0.125,0,0.1), \quad 1/2 < x/L_0 < 1.$$

*Case 2.* Strong shock wave with the initial condition

$$(\rho/\rho_0, u_x/u_0, p/p_0) = (1,0,1000), \quad 0 < x/L_0 \leqslant 1/2,$$

$$(\rho/\rho_0, u_x/u_0, p/p_0) = (1,0,0.01), \quad 1/2 < x/L_0 < 1.$$

Here $L_0$ is the reference length. In particular, for $\rho_0 = 1.165\ \mathrm{kg/m^3}$, $R = 287\ \mathrm{J/(kg\ K)}$, $T_0 = 303\ \mathrm{K}$, $\mu = 1.86 \times 10^{-5}\ \mathrm{kg/(m\ s)}$ (air under normal condition), and $L_0 = 2\ \mathrm{m}$, the mesh is specified by setting $\Delta x = \Delta y$, and $N_x \times N_y = 400 \times 5$, where $N_x$ and $N_y$ are the lattice numbers along the $x$ and $y$ directions, respectively. In the $x$ direction, $f_\alpha = f_\alpha^{eq}$ is set and the periodic boundary condition is imposed in the $y$ direction. The third-order IMEX Runge-Kutta scheme and the WENO scheme are used in the two cases. The characteristic time of the system is defined as $t_0 = L_0/u_0$ and the specific-heat ratio is set to be 1.4 (air) with $b = 5$ and the Prandtl number is set to be 0.71.

The profiles of the velocity, temperature, density, and pressure at $t = 0.1644 t_0$ for the Sod shock tube obtained from the simulations are presented in Figs. 2 and 3, where the theoretical solutions are represented with solid lines for comparison. In this case, we set $T_c = 2T_0$ and $\Delta t = 30\,000\ \mu/(\rho_0 R T_0)$ with CFL=0.92. The numerical results are found to be in excellent agreement with the theoretical ones for both models I and II.

The strong shock-wave problem, which has an extremely large pressure ratio, 100 000, is a very challenging problem for numerical methods. For this test, we set $T_c = 1000 T_0$ and $\Delta t = 1000\ \mu/(\rho_0 R T_0)$. The profiles of the velocity, temperature, density, and pressure at $t = 0.012 t_0$ are shown in Figs. 4 and 5. To sum up, the numerical results are well consistent with the theoretical results. However, there are some reasonable and noticeable deviations in density, velocity, and pressure profiles for both models I and II, and note that the results from model II are a little better than those from model I, which can be accepted considering the maximum Mach number is about 1.9.

### B. Double Mach reflection

The double-Mach-reflection problem has been used extensively as a test problem for comparing the performance of various numerical methods on problems involving strong

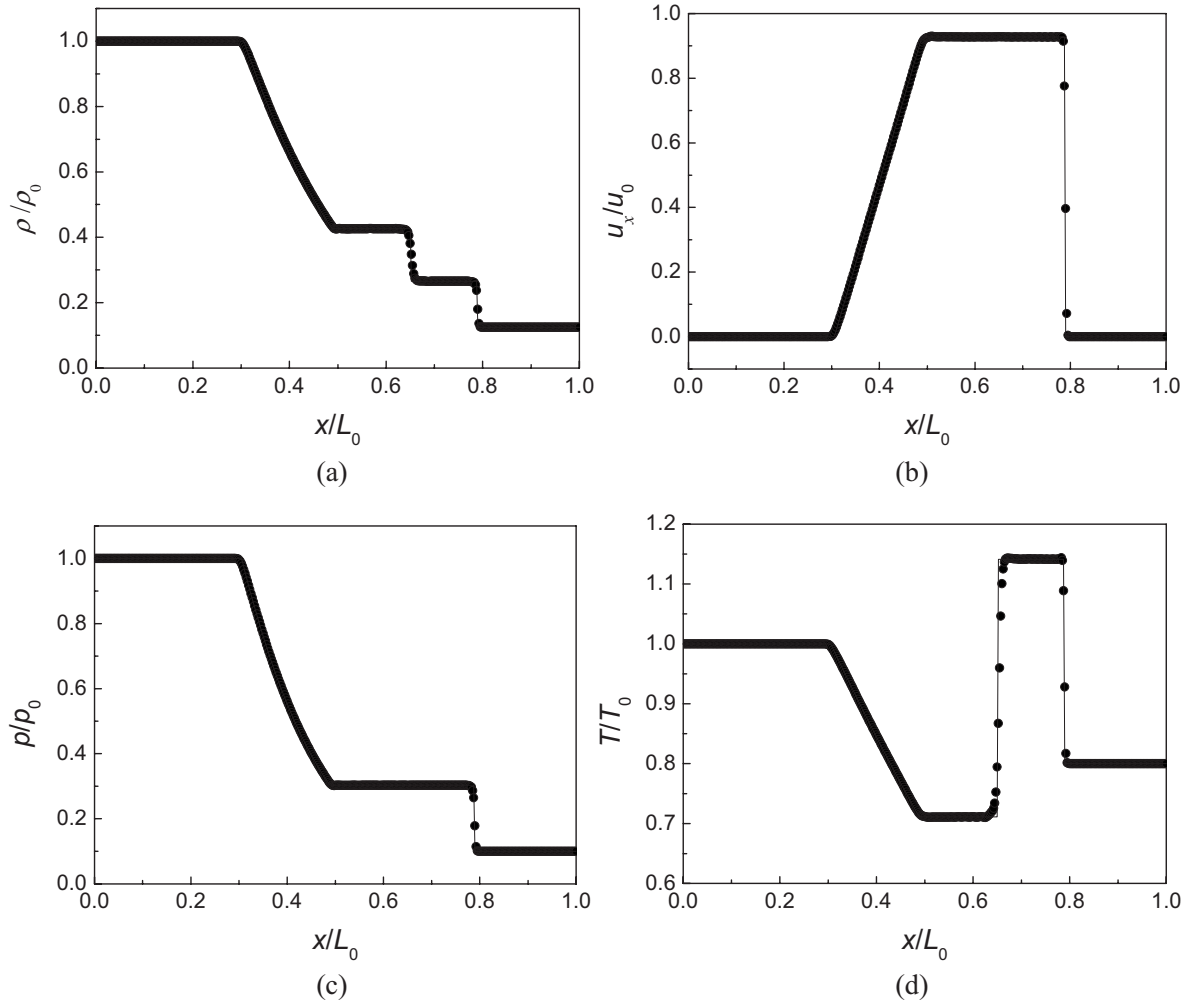


FIG. 2. Simulation of the Sod shock tube by mode I, comparisons between numerical and theoretical solutions of the Sod shock tube. (a) Density, (b) velocity, (c) pressure, and (d) temperature.

shocks. It is an unsteady shock reflection problem. A planar shock is incident on an oblique surface, with the surface at a 30° angle to the direction of propagation of the shock (Fig. 6). The fluid in front of the shock has zero velocity, and the shock Mach number is equal to 10 [22,26,38,39].

In this test, the computational domain is a rectangle of length 3 and height 1. This domain is divided into a 360 $\times$ 140 uniform mesh. The reflecting wall lies along the bottom of the domain, beginning at $x=1/6$. The shock makes a 60° angle with the $x$ axis and extends to the top of the domain at $y=1$. The short region from $x=0$ to $x=1/6$ along the bottom boundary at $y=0$ is always assigned values for the initial post-shock flow. This boundary condition forces the reflected shock to be attached to the reflecting wall. The left-hand boundary is also assigned values for the initial post-shock flow, and at the right-hand boundary, at $x=3$, the extrapolation technique is applied. The values along the top boundary are set to describe the exact motion of the initial Mach 10 shock; it means that this test uses a time-dependent physical boundary condition at the top boundary.

In the computation, we set $b=5$, $\mathrm{Pr}=0.71$, $T_c=85T_0$, and $\Delta t=4000\mu/(\rho_0 RT_0)$ with CFL=0.56. The second-order IMEX Runge-Kutta scheme and the TVD scheme are used in this test. The density and pressure contours at $t=860\Delta t$ are shown in Fig. 7. The distance between points $A$ and $B$ (see Fig. 6) is given by $|AB|=2\times(10u_0\times 860\Delta t)/\sqrt{3}\approx 2.15$. Complex features, such as oblique shocks and triple points, are well captured. The results agree very well with those obtained by using the upwind method [39] and the adaptive LBM at the Navier-Stokes level [26].

### C. Couette flow

Couette flow is a classical heat-transfer problem which can provide a good test of a new lattice Boltzmann model to describe viscous heat dissipation. Consider a viscous fluid flow between two infinite parallel flat plates, separated by a distance of $H$. The top plate at temperature $T_1$ moves at speed $U$, and the bottom plate at temperature $T_0$ is stationary. In a steady state, the temperature profiles satisfy the following relations when the variation of the viscosity and thermal conductivity is neglected:

$$T_1 = T_0\text{: } T - T_0 = \mathrm{Pr}\frac{U^2}{2c_p}\frac{y}{H}\left(1-\frac{y}{H}\right), \tag{71}$$

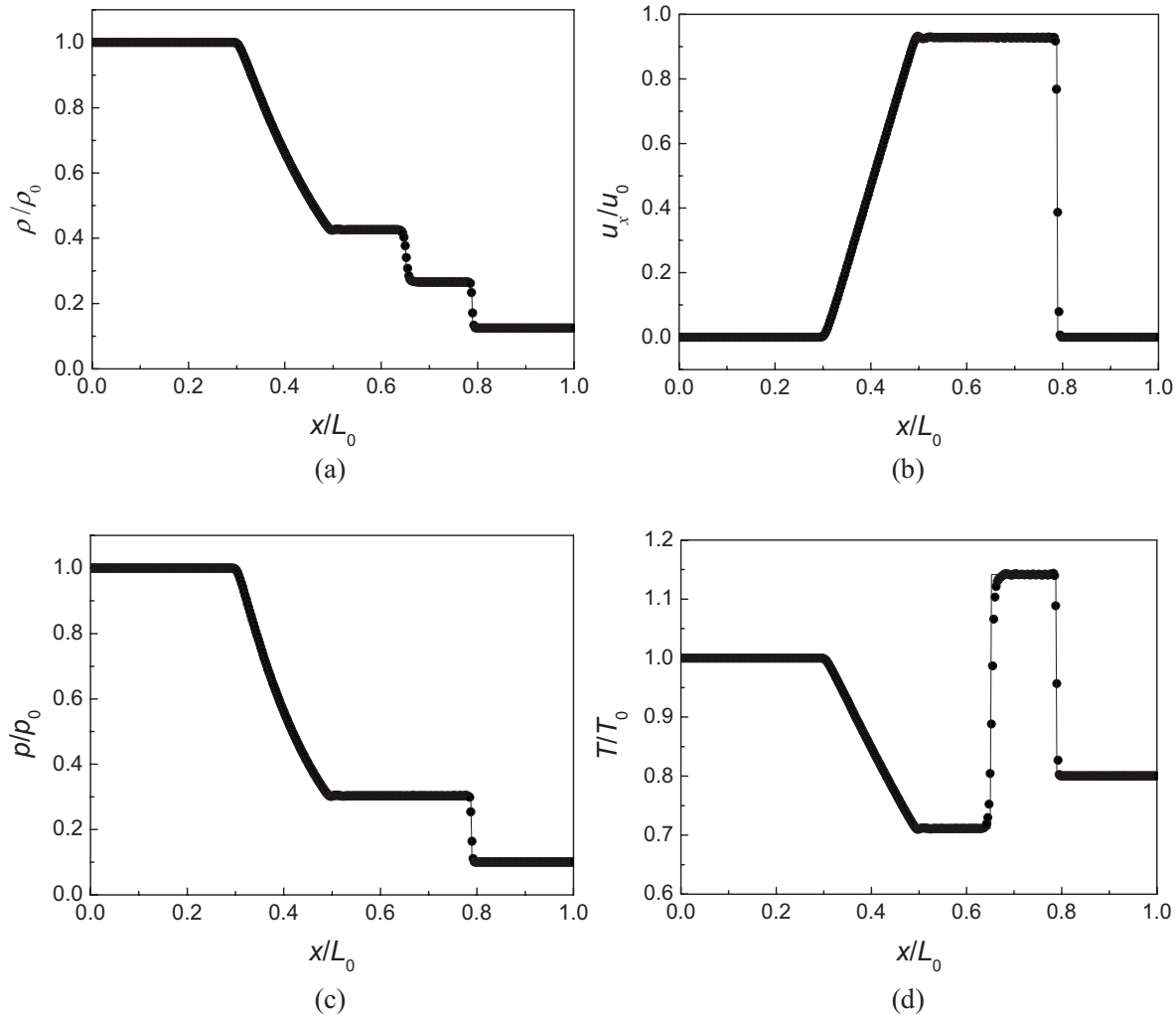


FIG. 3. Simulation of the Sod shock tube by mode II, comparisons between numerical and theoretical solutions of the Sod shock tube. (a) Density, (b) velocity, (c) pressure, and (d) temperature.

$$T_1 \neq T_0: \frac{T-T_0}{T_1-T_0} = \frac{y}{H} + \frac{\mathrm{PrEc}}{2}\frac{y}{H}\left(1-\frac{y}{H}\right), \tag{72}$$

$$\frac{u_x}{U} = \frac{y}{H} + \frac{2}{\pi}\sum_{n=1}^{\infty}\left[\frac{(-1)^n}{n}\exp\left(-n^2\pi^2\frac{\mu t}{\rho H^2}\right)\sin\left(\frac{n\pi y}{H}\right)\right], \tag{73}$$

where $y$ is the distance from the bottom boundary, $\mathrm{Pr}=\mu c_p/\lambda$ is the Prandtl number, and $\mathrm{Ec}=U^2/c_p(T_1-T_0)$ is the Eckert number.

As there is no shock wave or discontinuity in the Couette flow, Eqs. (69) and (70) are used in simulations. Moreover, in this test, the characteristic temperature $T_c$ can be set to be a value which is smaller than the maximum stagnation temperature to obtain a larger $\Delta t$, as long as numerical stability and accuracy are ensured. In the computation, a mesh $N_x \times N_y = 40 \times 40$ with $\Delta x = \Delta y$ is used for all simulations; a periodic boundary condition is applied to the inlet and outlet, and the nonequilibrium extrapolation method [37] is applied to the two plates.

The following numerical results are obtained from model I with $T_c = T_0$ unless otherwise mentioned. Dimensionless velocity profiles at various time steps for $T_1 = T_0$, $U = 0.5u_0$, $\gamma = 1.4$, and $\mathrm{Pr}=2$ are shown in Fig. 8. The numerical results exactly agree with the following analytical solution:

although Eqs. (69) and (70) only have first-order accuracy in time.

For the steady Couette flow, Fig. 9 shows dimensionless temperature profiles for $T_1 = T_0$, $U = u_0$, $\mathrm{Pr}=2$, and $\gamma = 5/3$, 7/5, and 9/7. Figure 10 shows the results for $T_1 = T_0$, $U = u_0$, $\gamma = 7/5$, and $\mathrm{Pr}=1$, 2, and 3, and analytical solutions are also presented for comparison. As shown, the numerical results agree very well with the analytical solutions.

Furthermore, we also conduct a simulation to measure the temperature profiles for $T_1 = (1+0.05)T_0$, $\gamma = 7/5$, $\mathrm{Pr}=3.5$, and $U = 0.5u_0$, $1.0u_0$, and $1.5u_0$. Figure 11 shows that our results obtained from model I are in excellent agreement with the analytical ones, even when the flow is supersonic. However, for high speed flows with $\mathrm{Ma} \geqslant 2$, which are often beyond the ability of model I, we suggest using model II.

Simulations of the Couette flow by model II are carried out for $T_1 = T_0$, $\mathrm{Pr}=2$, $\gamma = 7/5$, and $U = 5u_0$, $7u_0$, and $10u_0$

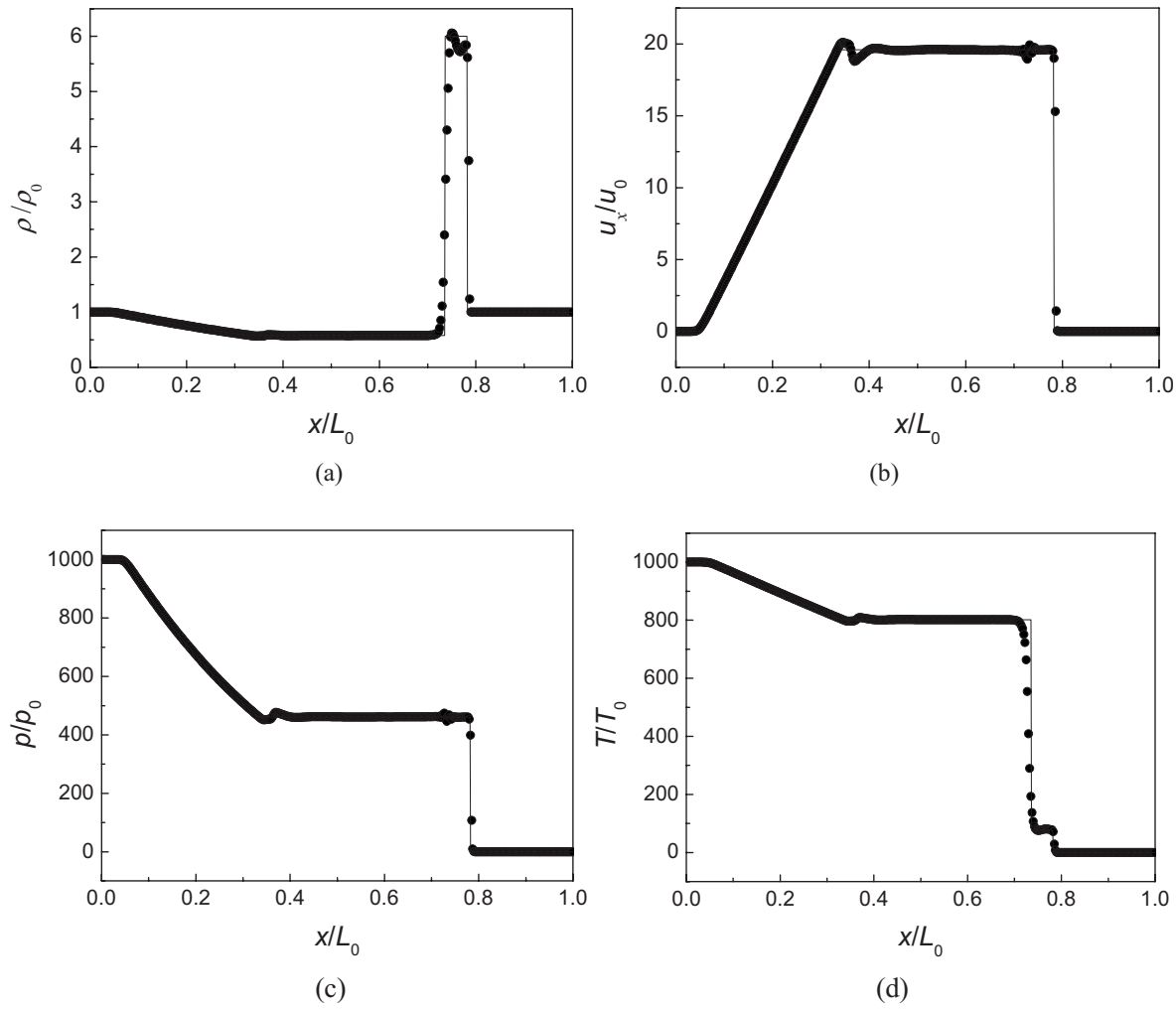


FIG. 4. Simulation of a strong shock wave by mode I, comparisons between numerical and theoretical solution of the Sod shock tube. (a) Density, (b) velocity, (c) pressure, and (d) temperature.

(Ma$\approx$8.45). $T_c$ is set to be $20T_0$, and the results are presented in Fig. 12. As can be seen there, high-speed viscous flows can be well simulated by model II.

## V. CONCLUSION

In this paper, we have developed a coupled DDF lattice Boltzmann method for compressible NS equations. In the method, the compressible continuity and momentum equations are recovered by a density distribution function based on a multispeed lattice, while the compressible energy equation is recovered by an energy distribution function. The coupling between the two distribution functions is established by using the thermal equation of state to make sure that the momentum and energy transports are coupled. Different from the existing lattice Boltzmann methods for compressible NS equations, the proposed method can easily make both the specific-heat ratio and the Prandtl number arbitrary. Moreover, in order to obtain high accuracy in time, a recently developed numerical technique for stiff problems, the so-called IMEX Runge-Kutta scheme, has been introduced to solve the discrete Boltzmann equations in the coupled DDF method. Constraints to recover the compressible NS equations also have been presented for the equilibrium distribution functions in this paper. In particular, two coupled DDF models have been designed: one is based on the conventional LBM in which the truncated Maxwellian equilibrium distribution function is used, and the other is based on a circular function and can be used for high-Mach-number flows. The models together with the method are well validated by the numerical simulations of the Riemann problem, the double-Mach-reflection problem, and the Couette flow with a range of specific-heat ratios and Prandtl numbers. The extension of the present method to three-dimensional space is under way.

## ACKNOWLEDGMENTS

This work was supported by the National Natural Science Fund for Distinguished Young Scholars from the National Natural Science Foundation of China (Grant No. 50425620) and National Basic Research Program of China (973 Program) (Grant No. 2007CB206902).

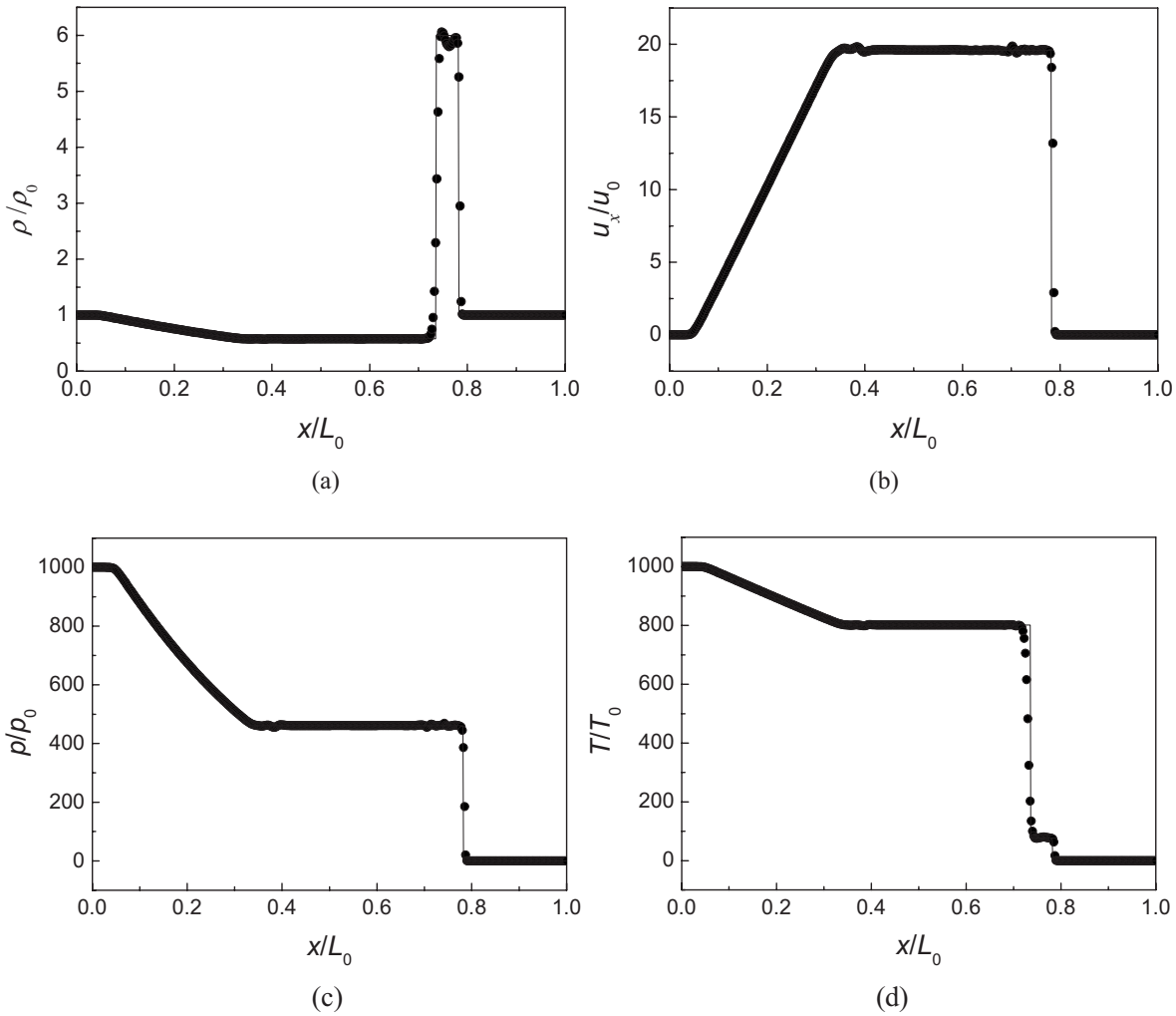


FIG. 5. Simulation of a strong shock wave by mode II, comparisons between numerical and theoretical solutions of the Sod shock tube. (a) Density, (b) velocity, (c) pressure, and (d) temperature.

## APPENDIX A: CHAPMAN-ENSKOG ANALYSIS OF THE EVOLUTION EQUATION FOR THE INTERNAL ENERGY DISTRIBUTION FUNCTION

We first expand the internal energy distribution function as

$$g_\alpha = g_\alpha^{eq} + Kg_\alpha^{(1)} + K^2 g_\alpha^{(2)} + \cdots . \tag{A1}$$

$g_\alpha^{(n)}$ is constrained by

$$\sum_\alpha g_\alpha^{(n)} = 0, \quad n = 1,2, \ldots . \tag{A2}$$

Substituting Eqs. (4a)–(4c) and Eq. (A1) into Eq. (34), we can obtain the following equations:

$$\frac{\partial g_\alpha^{eq}}{\partial t_1} + (\boldsymbol{e}_\alpha \cdot \boldsymbol{\nabla}_1) g_\alpha^{eq} = -\frac{g_\alpha^{(1)}}{\tau_g} - f_\alpha^{eq} q_{\alpha 1}, \tag{A3}$$

$$\frac{\partial g_\alpha^{eq}}{\partial t_2} + \left[\frac{\partial}{\partial t_1} + (\boldsymbol{e}_\alpha \cdot \boldsymbol{\nabla}_1)\right] g_\alpha^{(1)} = -\frac{g_\alpha^{(2)}}{\tau_g} - f_\alpha^{(1)} q_{\alpha 1} - f_\alpha^{eq} q_{\alpha 2}, \tag{A4}$$

where $q_{\alpha 1}$ and $q_{\alpha 2}$ are given by, respectively,

$$q_{\alpha 1} = (\boldsymbol{e}_\alpha - \boldsymbol{u}) \cdot \left[\frac{\partial \boldsymbol{u}}{\partial t_1} + (\boldsymbol{u} \cdot \boldsymbol{\nabla}_1)\boldsymbol{u}\right] + (\boldsymbol{e}_\alpha - \boldsymbol{u})(\boldsymbol{e}_\alpha - \boldsymbol{u}) : \boldsymbol{\nabla}_1 \boldsymbol{u}, \tag{A5}$$

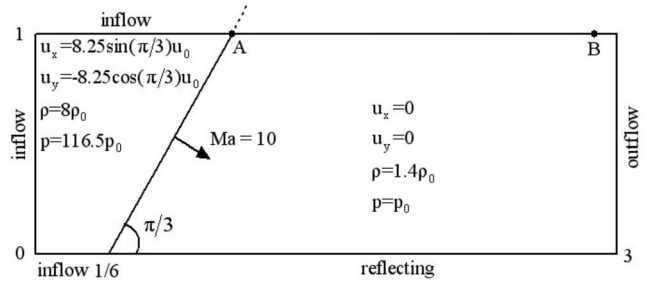


FIG. 6. Configuration of the double-Mach-reflection problem.

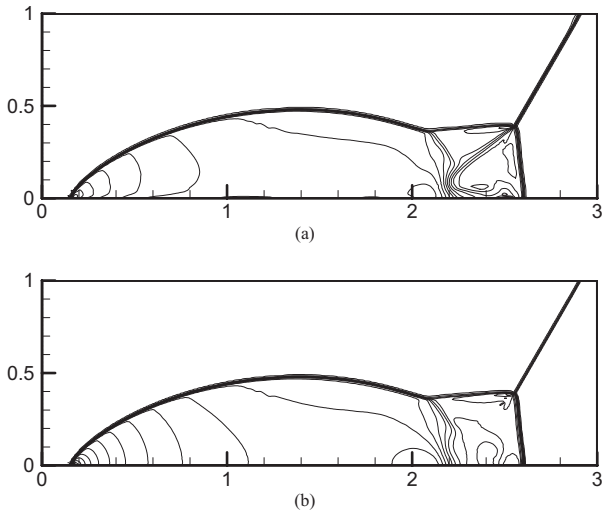


FIG. 7. Simulation of the double-Mach-reflection (Ma=10) problem by mode II, density (a) and pressure (b) contours.

$$q_{\alpha 2} = (\boldsymbol{e}_\alpha - \boldsymbol{u}) \cdot \frac{\partial \boldsymbol{u}}{\partial t_2}. \tag{A6}$$

Taking the summation of Eqs. (A3) and (A4) over velocity space, respectively, we have

$$\frac{\partial}{\partial t_1}(\rho c_v T) + \boldsymbol{\nabla}_1 \cdot (\rho c_v T \boldsymbol{u}) = -p \boldsymbol{\nabla}_1 \cdot \boldsymbol{u}, \tag{A7}$$

$$\frac{\partial}{\partial t_2}(\rho c_v T) + \sum_\alpha (\boldsymbol{e}_\alpha \cdot \boldsymbol{\nabla}_1) g_\alpha^{(1)} = -\sum_\alpha f_\alpha^{(1)} q_{\alpha 1} - \sum_\alpha f_\alpha^{eq} q_{\alpha 2}, \tag{A8}$$

where $c_v = bR/2$ is the specific heat at constant volume. From Eqs. (3a) and (3b), we can obtain

$$\sum_\alpha f_\alpha^{eq} q_{\alpha 2} = 0. \tag{A9}$$

From Eq. (5), we have

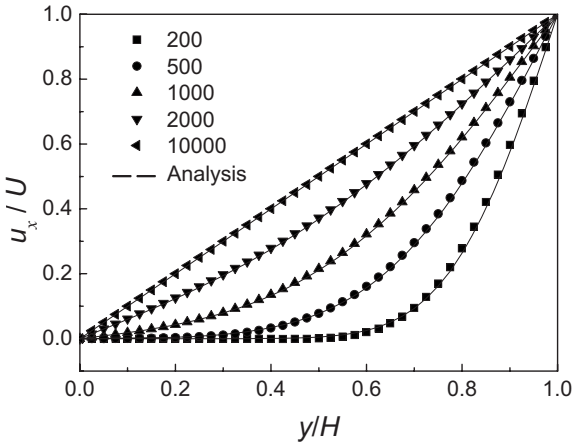


FIG. 8. Dimensionless velocity profiles in unsteady Couette flow for $T_1 = T_0$, $U = 0.5u_0$, $\gamma = 1.4$, and Pr=2 at various time steps.

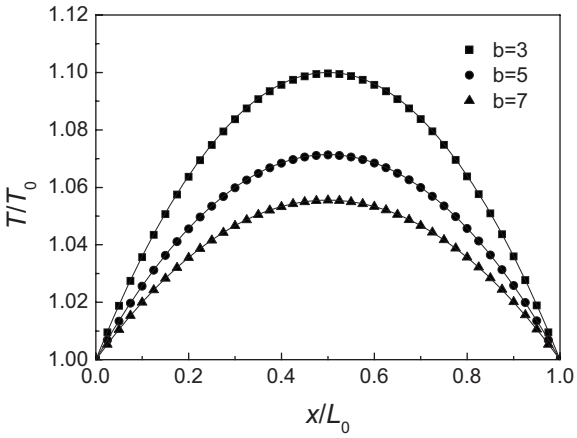


FIG. 9. Dimensionless temperature profiles in steady Couette flow for $T_1 = T_0$, $U = u_0$, Pr=2, and $\gamma = (b+2)/b$.

$$\sum_\alpha f_\alpha^{(1)} (\boldsymbol{e}_\alpha - \boldsymbol{u}) \cdot \left[ \frac{\partial \boldsymbol{u}}{\partial t_1} + (\boldsymbol{u} \cdot \boldsymbol{\nabla}_1) \boldsymbol{u} \right] = 0, \tag{A10}$$

$$\sum_\alpha f_\alpha^{(1)} (\boldsymbol{e}_\alpha - \boldsymbol{u})(\boldsymbol{e}_\alpha - \boldsymbol{u}) : \boldsymbol{\nabla}_1 \boldsymbol{u} = \sum_\alpha f_\alpha^{(1)} \boldsymbol{e}_\alpha \boldsymbol{e}_\alpha : \boldsymbol{\nabla}_1 \boldsymbol{u}. \tag{A11}$$

Then the following equation can be obtained:

$$\sum_\alpha f_\alpha^{(1)} q_{\alpha 1} = \sum_\alpha f_\alpha^{(1)} \boldsymbol{e}_\alpha \boldsymbol{e}_\alpha : \boldsymbol{\nabla}_1 \boldsymbol{u}. \tag{A12}$$

By using Eq. (A7) and noting that $p = \rho RT$ for an ideal gas, we can obtain

$$\frac{\partial p}{\partial t_1} = -\boldsymbol{\nabla}_1 \cdot (p \boldsymbol{u}) - \frac{2}{b} p \boldsymbol{\nabla}_1 \cdot \boldsymbol{u}. \tag{A13}$$

Then the following equation can be obtained [compared with Eqs. (14)–(18)]:

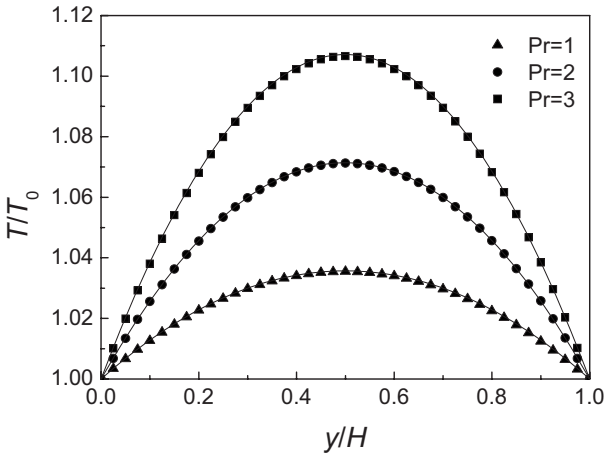


FIG. 10. Dimensionless temperature profiles in steady Couette flow for $T_1 = T_0$, $U = u_0$, $\gamma = 7/5$, and Pr=1, 2, and 3.

$$\sum_{\alpha} e_{\alpha i} e_{\alpha j} f_{\alpha}^{(1)} = -\tau_f p \left( \frac{\partial u_i}{\partial r_{1j}} + \frac{\partial u_j}{\partial r_{1i}} - \frac{2}{b} \frac{\partial u_k}{\partial r_{1k}} \delta_{ij} \right). \quad \text{(A14)}$$

From Eq. (A3), we have

$$\sum_{\alpha} (\boldsymbol{e}_{\alpha} \cdot \boldsymbol{\nabla}_1) g_{\alpha}^{(1)} = -\tau_g \sum_{\alpha} \frac{\partial}{\partial r_{1j}} \left[ \frac{\partial}{\partial t_1} (e_{\alpha j} g_{\alpha}^{eq}) + \frac{\partial}{\partial r_{1i}} (e_{\alpha i} e_{\alpha j} g_{\alpha}^{eq}) + f_{\alpha}^{eq} e_{\alpha j} q_{\alpha 1} \right]. \quad \text{(A15)}$$

By using Eqs. (3b)–(3d), we can obtain

$$\sum_{\alpha} f_{\alpha}^{eq} e_{\alpha j} (\boldsymbol{e}_{\alpha} - \boldsymbol{u}) \cdot \left[ \frac{\partial \boldsymbol{u}}{\partial t_1} + (\boldsymbol{u} \cdot \boldsymbol{\nabla}_1) \boldsymbol{u} \right] = p \left( \frac{\partial u_j}{\partial t_1} + u_i \frac{\partial u_j}{\partial r_{1i}} \right), \quad \text{(A16)}$$

$$\sum_{\alpha} f_{\alpha}^{eq} e_{\alpha j} (\boldsymbol{e}_{\alpha} - \boldsymbol{u})(\boldsymbol{e}_{\alpha} - \boldsymbol{u}) : \boldsymbol{\nabla}_1 \boldsymbol{u} = p u_j \frac{\partial u_k}{\partial r_{1k}}. \quad \text{(A17)}$$

With these results, we can obtain

$$\sum_{\alpha} f_{\alpha}^{eq} e_{\alpha j} q_{\alpha 1} = p \left( \frac{\partial u_j}{\partial t_1} + u_i \frac{\partial u_j}{\partial r_{1i}} \right) + p u_j \frac{\partial u_k}{\partial r_{1k}}. \quad \text{(A18)}$$

Combining Eq. (10) with Eq. (11) leads to

$$\frac{\partial u_j}{\partial t_1} = -u_i \frac{\partial u_j}{\partial r_{1i}} - \frac{1}{\rho} \frac{\partial p}{\partial r_{1j}}. \quad \text{(A19)}$$

From Eq. (A19) and noting that $p = \rho RT$, we have

$$\sum_{\alpha} f_{\alpha}^{eq} e_{\alpha j} q_{\alpha 1} = -RT \frac{\partial p}{\partial r_{1j}} + p u_j \frac{\partial u_k}{\partial r_{1k}}. \quad \text{(A20)}$$

Combining Eqs. (35b), (A7), and (A19), we have

$$\frac{\partial}{\partial t_1} \left( \sum_{\alpha} e_{\alpha j} g_{\alpha}^{eq} \right) = -u_j \frac{\partial}{\partial r_{1i}} \left( \rho \frac{b}{2} RT u_i \right) - p u_j \frac{\partial u_k}{\partial r_{1k}} - \rho \frac{b}{2} RT u_i \frac{\partial u_j}{\partial r_{1i}} - \frac{b}{2} RT \frac{\partial p}{\partial r_{1j}}. \quad \text{(A21)}$$

From Eq. (35c), we can obtain

$$\frac{\partial}{\partial r_{1i}} \left( \sum_{\alpha} e_{\alpha i} e_{\alpha j} g_{\alpha}^{eq} \right) = u_i u_j \frac{\partial}{\partial r_{1i}} \left( \rho \frac{b}{2} RT \right) + \rho \frac{b}{2} RT u_j \frac{\partial u_i}{\partial r_{1i}} + \rho \frac{b}{2} RT u_i \frac{\partial u_j}{\partial r_{1i}} + \left( \frac{b+2}{2} \right) RT \frac{\partial p}{\partial r_{1j}} + \left( \frac{b+2}{2} \right) Rp \frac{\partial T}{\partial r_{1j}}. \quad \text{(A22)}$$

Substituting Eqs. (A20)–(A22) into Eq. (A15), we can obtain

$$\sum_{\alpha} (\boldsymbol{e}_{\alpha} \cdot \boldsymbol{\nabla}_1) g_{\alpha}^{(1)} = -\tau_g \frac{\partial}{\partial r_{1j}} \left[ \left( \frac{b+2}{2} \right) Rp \frac{\partial T}{\partial r_{1j}} \right]. \quad \text{(A23)}$$

Combining Eqs. (A9), (A12), and (A23), we can rewrite Eq. (A8) as

$$\frac{\partial}{\partial t_2} (\rho \varepsilon) = \tau_g \frac{\partial}{\partial r_{1j}} \left[ \left( \frac{b+2}{2} \right) Rp \frac{\partial T}{\partial r_{1j}} \right] + \sum_{\alpha} f_{\alpha}^{(1)} \boldsymbol{e}_{\alpha} \boldsymbol{e}_{\alpha} : \boldsymbol{\nabla}_1 \boldsymbol{u}. \quad \text{(A24)}$$

Finally, Combining Eqs. (A7) and (A24) together with $\partial_t = K\partial_{t_1} + K^2 \partial_{t_2}$, we can obtain the internal energy conservation equation

$$\frac{\partial}{\partial t} (\rho c_v T) + \boldsymbol{\nabla} \cdot (\rho c_v T \boldsymbol{u}) = \boldsymbol{\nabla} \cdot (\lambda \boldsymbol{\nabla} T) + \boldsymbol{\Pi}' : \boldsymbol{\nabla} \boldsymbol{u} - p \boldsymbol{\nabla} \cdot \boldsymbol{u}, \quad \text{(A25)}$$

where $\lambda = \tau_g (c_v + R) p$ is the thermal conductivity and $\Pi'$ is given by

$$\boldsymbol{\Pi}' = \mu \left[ \boldsymbol{\nabla} \boldsymbol{u} + (\boldsymbol{\nabla} \boldsymbol{u})^{\mathsf{T}} - \frac{2}{D} (\boldsymbol{\nabla} \cdot \boldsymbol{u}) \mathbf{I} \right] + \mu_B (\boldsymbol{\nabla} \cdot \boldsymbol{u}) \mathbf{I}, \quad \text{(A26)}$$

where $\mu = \tau_f p$ is the dynamic viscosity, $\mu_B = 2(1/D - 1/b)\tau_f p$ is the bulk viscosity, and $\mathbf{I}$ is the unit tensor.

## APPENDIX B: CHAPMAN-ENSKOG ANALYSIS OF THE EVOLUTION EQUATION FOR THE TOTAL ENERGY DISTRIBUTION FUNCTION

Similarly, we expand the total energy distribution function as

$$h_{\alpha} = h_{\alpha}^{eq} + K h_{\alpha}^{(1)} + K^2 h_{\alpha}^{(2)} + \cdots. \quad \text{(B1)}$$

Combining Eq. (41a) with Eq. (42), we can obtain

$$\sum_{\alpha} h_{\alpha}^{(n)} = 0, \quad n = 1, 2, \ldots. \quad \text{(B2)}$$

Substituting Eqs. (4a)–(4c) and Eq. (B1) into Eq. (40), we can obtain a series of equations in terms of the order of $K$:

$$K^1 : \frac{\partial h_{\alpha}^{eq}}{\partial t_1} + (\boldsymbol{e}_{\alpha} \cdot \boldsymbol{\nabla}_1) h_{\alpha}^{eq} = -\frac{h_{\alpha}^{(1)}}{\tau_h} + (\boldsymbol{e}_{\alpha} \cdot \boldsymbol{u}) \frac{f_{\alpha}^{(1)}}{\tau_{hf}}, \quad \text{(B3)}$$

$$K^2 : \frac{\partial h_{\alpha}^{eq}}{\partial t_2} + \left[ \frac{\partial}{\partial t_1} + (\boldsymbol{e}_{\alpha} \cdot \boldsymbol{\nabla}_1) \right] h_{\alpha}^{(1)} = -\frac{h_{\alpha}^{(2)}}{\tau_h} + (\boldsymbol{e}_{\alpha} \cdot \boldsymbol{u}) \frac{f_{\alpha}^{(2)}}{\tau_{hf}}. \quad \text{(B4)}$$

Taking the summation of Eqs. (B3) and (B4) over velocity space, respectively, we have

$$\frac{\partial}{\partial t_1} (\rho E) + \boldsymbol{\nabla}_1 \cdot [(\rho E + p) \boldsymbol{u}] = 0, \quad \text{(B5)}$$

$$\frac{\partial}{\partial t_2} (\rho E) + \sum_{\alpha} (\boldsymbol{e}_{\alpha} \cdot \boldsymbol{\nabla}_1) h_{\alpha}^{(1)} = 0. \quad \text{(B6)}$$

Multiplying Eq. (B3) by $e_{\alpha j}$ and then taking the summation over velocity space, we have

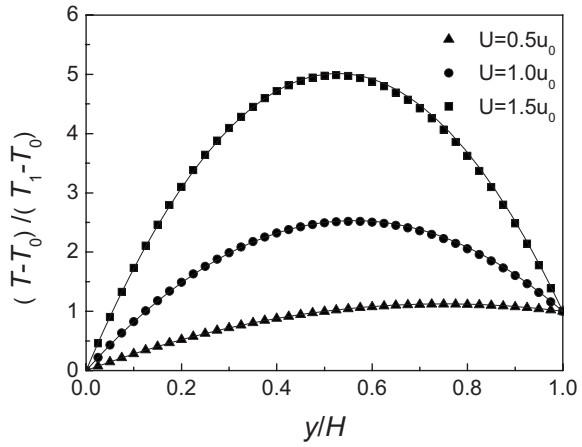


FIG. 11. Dimensionless temperature profiles in steady Couette flow for $T_1=(1+0.05)T_0$, Pr=3.5, $\gamma=7/5$, and $U=0.5u_0$, $u_0$, and $1.5u_0$.

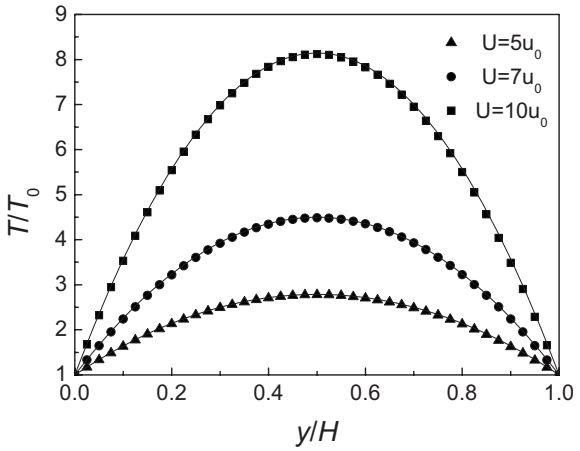


FIG. 12. Simulation of steady Couette flow by mode II, dimensionless temperature profiles for $T_1=T_0$, Pr=2, $\gamma=7/5$, and $U=5u_0$, $7u_0$, and $10u_0$.

$$\frac{\partial}{\partial t_1}\left(\sum_\alpha e_{\alpha j}h_\alpha^{eq}\right)+\frac{\partial}{\partial r_{1i}}\left(\sum_\alpha e_{\alpha i}e_{\alpha j}h_\alpha^{eq}\right)=-\frac{1}{\tau_h}\sum_\alpha e_{\alpha j}h_\alpha^{(1)}+\frac{1}{\tau_{hf}}u_i\sum_\alpha e_{\alpha i}e_{\alpha j}f_\alpha^{(1)}. \tag{B7}$$

Using Eqs. (41b) and (41c), we have

$$\sum_\alpha e_{\alpha j}h_\alpha^{(1)}=-\tau_h\left\{\frac{\partial}{\partial t_1}[(\rho E+p)u_j]+\frac{\partial}{\partial r_{1i}}[(\rho E+2p)u_iu_j+p(E+RT)\delta_{ij}]\right\}+\frac{\tau_h}{\tau_{hf}}u_i\sum_\alpha e_{\alpha i}e_{\alpha j}f_\alpha^{(1)}. \tag{B8}$$

Combining Eq. (10) with Eq. (11) leads to

$$\frac{\partial u_j}{\partial t_1}=-u_i\frac{\partial u_j}{\partial r_{1i}}-\frac{1}{\rho}\frac{\partial p}{\partial r_{1j}}. \tag{B9}$$

From Eqs. (B5) and (B9), we can get

$$\frac{\partial}{\partial t_1}(\rho Eu_j)=-\rho Eu_i\frac{\partial u_j}{\partial r_{1i}}-E\frac{\partial p}{\partial r_{1j}}-u_j\frac{\partial}{\partial r_{1i}}[(\rho E+p)u_i]. \tag{B10}$$

In order to derive the expression for $\partial(pu_j)/\partial t_1$, we rewrite the left-hand side of Eq. (B5) as follows:

$$\begin{aligned}&\frac{\partial}{\partial t_1}\left(\frac{1}{2}\rho u^2+\rho\frac{b}{2}RT\right)+\frac{\partial}{\partial r_{1k}}\left(\frac{1}{2}\rho u^2u_k+\rho\frac{b}{2}RTu_k+pu_k\right)\\&=u_j\frac{\partial}{\partial t_1}(\rho u_j)+\frac{\partial}{\partial t_1}\left(\rho\frac{b}{2}RT\right)+u_j\frac{\partial}{\partial r_{1k}}(\rho u_ku_j)+\frac{\partial}{\partial r_{1k}}\left(\rho\frac{b}{2}RTu_k\right)+p\frac{\partial u_k}{\partial r_{1k}}+u_k\frac{\partial p}{\partial r_k}\\&=u_j\left[\frac{\partial}{\partial t_1}(\rho u_j)+\frac{\partial}{\partial r_{1k}}(\rho u_ku_j)+\frac{\partial p}{\partial r_{1j}}\right]+\frac{\partial}{\partial t_1}\left(\rho\frac{b}{2}RT\right)+\frac{\partial}{\partial r_{1k}}\left(\rho\frac{b}{2}RTu_k\right)+p\frac{\partial u_k}{\partial r_{1k}}.\end{aligned}$$

The relation $u_k\partial p/\partial r_{1k}=u_j\partial p/\partial r_{1j}$ is used in the above derivation. Then, using Eq. (11), we can obtain

$$\frac{\partial p}{\partial t_1}=-\frac{\partial}{\partial r_{1k}}(pu_k)-\frac{2}{b}p\frac{\partial u_k}{\partial r_{1k}}. \tag{B11}$$

Combining Eqs. (B9) with (B11), we have

$$\frac{\partial}{\partial t_1}(pu_j)=-pu_i\frac{\partial u_j}{\partial r_{1i}}-RT\frac{\partial p}{\partial r_{1j}}-u_j\frac{\partial}{\partial r_{1k}}(pu_k)-(\gamma-1)pu_j\frac{\partial u_k}{\partial r_{1k}}. \tag{B12}$$

Then, substituting Eqs. (B10) and (B12) into Eq. (B8), we have

$$\sum_\alpha e_{\alpha j}h_\alpha^{(1)}=-\tau_h\left[pu_i\frac{\partial u_i}{\partial r_{1j}}+pu_i\frac{\partial u_j}{\partial r_{1i}}+(c_v+R)p\frac{\partial T}{\partial r_{1j}}-(\gamma-1)pu_i\delta_{ij}\frac{\partial u_k}{\partial r_{1k}}\right]+\frac{\tau_h}{\tau_{hf}}u_i\sum_\alpha e_{\alpha i}e_{\alpha j}f_\alpha^{(1)}. \tag{B13}$$

From Eq. (B11), $\Sigma_\alpha e_{\alpha i}e_{\alpha j}f_\alpha^{(1)}$ now is given by [compared with Eqs. (14)–(18)]

$$\sum_\alpha e_{\alpha i}e_{\alpha j}f_\alpha^{(1)}=-\tau_fp\left(\frac{\partial u_i}{\partial r_{1j}}+\frac{\partial u_j}{\partial r_{1i}}-(\gamma-1)\frac{\partial u_k}{\partial r_{1k}}\delta_{ij}\right). \tag{B14}$$

Thus, we can rewrite Eq. (B13) as

$$\sum_\alpha e_{\alpha j}h_\alpha^{(1)}=-\left(\frac{\tau_f\tau_h}{\tau_{hf}}+\tau_h\right)\left[pu_i\frac{\partial u_i}{\partial r_{1j}}+pu_i\frac{\partial u_j}{\partial r_{1i}}-(\gamma-1)pu_i\delta_{ij}\frac{\partial u_k}{\partial r_{1k}}\right]-\tau_h(c_v+R)p\frac{\partial T}{\partial r_{1j}}. \tag{B15}$$

Finally, combining Eqs. (B5), (B6), and (B15) and noting that $\tau_f\tau_h/\tau_{hf}+\tau_h=\tau_f$, we can obtain the compressible energy equation

$$\frac{\partial}{\partial t}(\rho E) + \nabla \cdot [(\rho E + p)\boldsymbol{u}] = \nabla \cdot (\lambda \nabla T) + \nabla \cdot (\boldsymbol{u} \cdot \boldsymbol{\Pi}'), \tag{B16}$$

where $\lambda = \tau_h(c_v + R)p$ is the thermal conductivity and $\Pi'$ is given by Eq. (A26).

## APPENDIX C: THE CONSTRAINTS FOR $\varpi_\alpha$

From Eq. (54) and using Eq. (3), we have

$$\begin{aligned}\sum_\alpha h_\alpha^{eq} &= \sum_\alpha \left( E f_\alpha^{eq} + (\boldsymbol{e}_\alpha - \boldsymbol{u}) \cdot \boldsymbol{u} f_\alpha^{eq} + \varpi_\alpha \frac{p}{\tilde{c}^2} RT \right) \\ &= \rho E + \sum_\alpha (e_{\alpha j} - u_j) u_j f_\alpha^{eq} + \sum_\alpha \varpi_\alpha \frac{p}{\tilde{c}^2} RT \\ &= \rho E + 0 + \sum_\alpha \varpi_\alpha \frac{p}{\tilde{c}^2} RT,\end{aligned}$$

$$\begin{aligned}\sum_\alpha e_{\alpha i} h_\alpha^{eq} &= \sum_\alpha e_{\alpha i} \left( E f_\alpha^{eq} + (\boldsymbol{e}_\alpha - \boldsymbol{u}) \cdot \boldsymbol{u} f_\alpha^{eq} + \varpi_\alpha \frac{p}{\tilde{c}^2} RT \right) = E \sum_\alpha e_{\alpha i} f_\alpha^{eq} + \sum_\alpha e_{\alpha i} (e_{\alpha j} - u_j) u_j f_\alpha^{eq} + \sum_\alpha e_{\alpha i} \varpi_\alpha \frac{p}{\tilde{c}^2} RT = \rho E u_i \\ &+ \sum_\alpha e_{\alpha i} e_{\alpha j} u_j f_\alpha^{eq} - \sum_\alpha e_{\alpha i} u_j^2 f_\alpha^{eq} + \sum_\alpha e_{\alpha i} \varpi_\alpha \frac{p}{\tilde{c}^2} RT = \rho E u_i + u_j (\rho u_i u_j + p \delta_{ij}) - u_j^2 \rho u_i + \sum_\alpha e_{\alpha i} \varpi_\alpha \frac{p}{\tilde{c}^2} RT = \rho E u_i + p u_i \\ &+ \sum_\alpha e_{\alpha i} \varpi_\alpha \frac{p}{\tilde{c}^2} RT,\end{aligned}$$

$$\begin{aligned}\sum_\alpha e_{\alpha i} e_{\alpha j} h_\alpha^{eq} &= \sum_\alpha e_{\alpha i} e_{\alpha j} \left( E f_\alpha^{eq} + (\boldsymbol{e}_\alpha - \boldsymbol{u}) \cdot \boldsymbol{u} f_\alpha^{eq} + \varpi_\alpha \frac{p}{\tilde{c}^2} RT \right) = E \sum_\alpha e_{\alpha i} e_{\alpha j} f_\alpha^{eq} + \sum_\alpha e_{\alpha i} e_{\alpha j} (e_{\alpha k} - u_k) u_k f_\alpha^{eq} + \sum_\alpha e_{\alpha i} e_{\alpha j} \varpi_\alpha \frac{p}{\tilde{c}^2} RT \\ &= \rho E u_i u_j + p E \delta_{ij} + \sum_\alpha e_{\alpha i} e_{\alpha j} e_{\alpha k} u_k f_\alpha^{eq} - \sum_\alpha e_{\alpha i} e_{\alpha j} u_k^2 f_\alpha^{eq} + \sum_\alpha e_{\alpha i} e_{\alpha j} \varpi_\alpha \frac{p}{\tilde{c}^2} RT = \rho E u_i u_j + p E \delta_{ij} + u_k [\rho u_i u_j u_k + p(u_k \delta_{ij} \\ &+ u_j \delta_{ik} + u_i \delta_{jk})] - (\rho u_i u_j + p \delta_{ij}) u_k^2 + \sum_\alpha e_{\alpha i} e_{\alpha j} \varpi_\alpha \frac{p}{\tilde{c}^2} RT = \rho E u_i u_j + p E \delta_{ij} + 2 p u_i u_j + \sum_\alpha e_{\alpha i} e_{\alpha j} \varpi_\alpha \frac{p}{\tilde{c}^2} RT.\end{aligned}$$

Finally, comparing the above equations with Eq. (41), we can obtain the constraints for $\varpi_\alpha$:

$$\sum_\alpha \varpi_\alpha \frac{p}{\tilde{c}^2} RT = 0, \tag{C1a}$$

$$\sum_\alpha e_{\alpha i} \varpi_\alpha \frac{p}{\tilde{c}^2} RT = 0, \tag{C1b}$$

$$\sum_\alpha e_{\alpha i} e_{\alpha j} \varpi_\alpha \frac{p}{\tilde{c}^2} RT = pRT \delta_{ij}. \tag{C1c}$$

## APPENDIX D: COEFFICIENTS OF THE IMEX RUNGE-KUTTA SCHEMES

The IMEX Runge-Kutta schemes can be represented by a double Butcher's tableau

$$\begin{array}{c|c} \tilde{\boldsymbol{a}} & \\ \hline & \tilde{\boldsymbol{w}}^{\mathrm{T}} \end{array} \qquad \begin{array}{c|c} \boldsymbol{a} & \\ \hline & \boldsymbol{w}^{\mathrm{T}} \end{array}$$

second-order scheme

| | | |
|---|---|---|
| 0 | 0 | 0 |
| 0 | 0 | 0 |
| 0 | 1 | 0 |
| 0 | 1/2 | 1/2 |

| | | |
|---|---|---|
| 1/2 | 0 | 0 |
| −1/2 | 1/2 | 0 |
| 0 | 1/2 | 1/2 |
| 0 | 1/2 | 1/2 |

third-order scheme

| | | | |
|---|---|---|---|
| 0 | 0 | 0 | 0 |
| 0 | 0 | 0 | 0 |
| 0 | 1 | 0 | 0 |
| 0 | 1/4 | 1/4 | 0 |
| 0 | 1/6 | 1/6 | 2/3 |

| | | | |
|---|---|---|---|
| $\chi$ | 0 | 0 | 0 |
| $-\chi$ | $\chi$ | 0 | 0 |
| 0 | $1-\chi$ | $\chi$ | 0 |
| $\chi$ | $\zeta$ | $1/2-\beta-\zeta-\chi$ | $\chi$ |
| 0 | 1/6 | 1/6 | 2/3 |

$$\chi = 0.24169426078821, \quad \beta = 0.06042356519705, \quad \zeta = 0.12915286960590.$$


[1] S. Chen and G. D. Doolen, Annu. Rev. Fluid Mech. **30**, 329 (1998).
[2] D. Yu, R. Mei, L.-S. Luo, and W. Shyy, Prog. Aerosp. Sci. **39**, 329 (2003).
[3] S. Succi. *The Lattice Boltzmann Equation for Fluid Dynamics and Beyond* (Clarendon Press, Oxford, 2001).
[4] P. Lallemand and L.-S. Luo, Phys. Rev. E **68**, 036706 (2003).
[5] J. G. M. Eggels and J. A. Somers, Int. J. Heat Fluid Flow **16**, 357 (1995).
[6] X. Shan, Phys. Rev. E **55**, 2780 (1997).
[7] F. J. Alexander, S. Chen, and J. D. Sterling, Phys. Rev. E **47**, R2249 (1993).
[8] Y. H. Qian, J. Sci. Comput. **8**, 231 (1993).
[9] Y. Chen, H. Ohashi, and M. Akiyama, Phys. Rev. E **50**, 2776 (1994).
[10] Y. Chen, H. Ohashi, and M. Akiyama, J. Sci. Comput. **12**, 169 (1997).
[11] T. Kataoka and M. Tsutahara, Phys. Rev. E **69**, 035701(R) (2004).
[12] G. Vahala, P. Pavlo, L. Vahala, and N. S. Martys, Int. J. Mod. Phys. C **9**, 1247 (1998).
[13] P. Lallemand and L.-S. Luo, Int. J. Mod. Phys. C **17**, 41 (2003).
[14] X. He, S. Chen, and G. D. Doolen, J. Comput. Phys. **146**, 282 (1998).
[15] Z. L. Guo, B. C. Shi, and C. G. Zheng, Int. J. Numer. Methods Fluids **39**, 325 (2002).
[16] Y. Peng, C. Shu, and Y. T. Chew, Phys. Rev. E **68**, 026701 (2003).
[17] Y. Shi, T. S. Zhao, and Z. L. Guo, Phys. Rev. E **70**, 066310 (2004).
[18] Z. Guo, C. Zheng, B. Shi, and T. S. Zhao, Phys. Rev. E **75**, 036704 (2007).
[19] Guangwu Yan, Yaosong Chen, and Shouxin Hu, Phys. Rev. E **59**, 454 (1999).
[20] F. L. Hinton, M. N. Rosenbluth, S. K. Wong, Y. R. Lin-Liu, and R. L. Miller, Phys. Rev. E **63**, 061212 (2001).
[21] W. Shi, W. Shyy, and R. Mei, Numer. Heat Transfer, Part B **40**, 1 (2001).
[22] K. Qu, C. Shu, and Y. T. Chew, Phys. Rev. E **75**, 036706 (2007).
[23] A. Renda, G. Bella, S. Succi, and I. V. Karlin, Europhys. Lett. **41**, 279 (1998).
[24] C. Sun, Phys. Rev. E **58**, 7283 (1998).
[25] C. Sun, Phys. Rev. E **61**, 2645 (2000).
[26] C. Sun, J. Comput. Phys. **161**, 70 (2000).
[27] C. Sun and A. T. Hsu, Phys. Rev. E **68**, 016303 (2003).
[28] C. Sun and A. T. Hsu, Comput. Fluids **33**, 1363 (2004).
[29] L. Pareschi1 and G. Russo, J. Sci. Comput. **25**, 129 (2005).
[30] S. Pieraccini and G. Puppo, J. Sci. Comput. **32**, 1 (2007).
[31] Y. Wang, Y. L. He, T. S. Zhao, G. H. Tang, and W. Q. Tao, Int. J. Mod. Phys. C (to be published).
[32] G. S. Jiang and C. W. Shu, J. Comput. Phys. **126**, 202 (1996).
[33] S. Chen, H. Chen, D. Martínez, and W. Matthaeus, Phys. Rev. Lett. **67**, 3776 (1991).
[34] Y. H. Qian, D. d'Humières, and P. Lallemand, Europhys. Lett. **17**, 479 (1992).
[35] K. Xu, J. Comput. Phys. **171**, 289 (2001).
[36] K. Xu and L.-S. Luo, Int. J. Mod. Phys. C **9**, 1177 (1998).
[37] Z. Guo, C. Zheng, and B. Shi, Phys. Fluids **14**, 2007 (2002).
[38] P. Woodward and P. Colella, J. Comput. Phys. **54**, 115 (1984).
[39] P. Colella, J. Comput. Phys. **87**, 171 (1990).